Aalto University
School of Science

Jukka Kärkimaa

Sliding friction of rubber on self-affine fractal surfaces

Master´s thesis submitted in partial fulfillment of the requirements for the degree of Master of Science in Technology in the Degree Programme in Engineering Physics and Mathematics.

Espoo, 24.10.2013

Supervisor: Professor Adam Foster

Instructor: D.Sc. (Tech.) Ari Tuononen

Aalto University School of Science	ABSTRACT OF THE MASTER'S THESIS

Author: Jukka Kärkimaa

Title: Sliding friction of rubber on self-affine fractal surfaces

Title in Finnish: Kumin liukukitka itseaffiinisilla fraktaalipinnoilla

Degree Programme: Degree Programme in Engineering Physics and Mathematics

Major subject: Engineering Physics F3005	Minor subject: Information and Computer Science IL3010

Chair (code): Tfy-105 Computational Physics

Supervisor: Prof. Adam Foster	Instructor: D.Sc. (Tech.) Ari Tuononen

The sliding friction of rubber differs from that of many other materials as its internal friction is exceptionally high. This is due to a high loss modulus and a particularly low elastic modulus above the glass transition temperature of rubber. The viscoelastic properties of rubber are temperature and frequency dependent. In addition to internal friction, the sliding friction of rubber can be partly attributed to adhesion losses.

In a slider-substrate system formed by a rubber block sliding on a hard rough substrate, the substrate asperities will exert time-dependent deformations on the rubber surface resulting in viscoelastic energy dissipation in the rubber, which contributes to the sliding friction. The perturbation frequency in the rubber block depends on the surface roughness of the substrate and the sliding speed. The surface roughness of many natural surfaces can be described as self-affine fractal. The advantage of a self-affine fractal treatment of a surface for a sliding friction model is the large range of roughness length scales which are incorporated and whose contribution to the sliding friction can thus be considered.

This thesis consists of experimental and computational study on the sliding friction exhibited by a slider-substrate system of a tyre rubber block sliding on an asphalt surface. The sliding friction coefficient as a function of temperature and sliding speed was measured for such a system in a climate chamber. The measured temperature and sliding speed ranges were from -8°C to +32°C and from 1 mm/s to 1 m/s, respectively. Furthermore, the experimental parameters describing the asphalt surface roughness, and the experimental data for the viscoelastic modulus of the rubber samples provided by the manufacturer were incorporated in the computational model.

The sliding friction theory implemented in the thesis is novel as it takes into account the effect from the abrupt rise of local temperatures in the rubber slider due to internal friction. It is increasingly important to consider this effect at sliding speeds over 1 cm/s, where the temperature rise in the rubber becomes significant.

The prediction of the implemented model for the sliding friction coefficient as a function of sliding speed was found to be qualitatively correct when comparing to the experiments performed at temperatures of +21°C and +32°C with sliding speeds from 1 mm/s to 1 m/s. However, the model seemed to exaggerate the maximum friction level many times. The inconsistency between the experiment and the model was suggested to lie in differences in the experimental conditions, such as humidity and the resulting water-layer on the surfaces, which are not considered in the model. Moreover, a relatively too low friction level, predicted by the model for sliding speeds below 1 cm/s, was attributed to such energy dissipation mechanisms (eg. shearing, crack opening) which are excluded from the model. Taking the rise of local temperatures in the rubber into account, the loss tangent was found to qualitatively predict the sliding friction level at least up to a sliding speed of 1 m/s. The asphalt surface was confirmed to be self-affine fractal by the profilometry measurement.

Date: 24.10.2013	Language: English	Number of pages: 59 + 17

Keywords: Rubber, sliding friction, surface roughness, self-affinity

Aalto-yliopisto Perustieteiden korkeakoulu	DIPLOMITYÖN TIIVISTELMÄ
Tekijä: Jukka Kärkimaa	
Työn nimi: Kumin liukukitka itseaffiinisilla fraktaalipinnoilla	
Title in English: Sliding friction of rubber on self-affine fractal surfaces	
Tutkinto-ohjelma: Teknillisen fysiikan ja matematiikan tutkinto-ohjelma	
Pääaine: Teknillinen fysiikka F3005	Sivuaine: Tietojenkäsittelytiede IL3010
Opetusyksikön (ent. professuuri) koodi: Tfy-105 Laskennallinen fysiikka	
Työn valvoja: Prof. Adam Foster	Työn ohjaaja(t): TkT Ari Tuononen

Kumin liukukitka eroaa muiden materiaalien liukukitkasta sisäisen kitkan suhteen, joka kumilla on poikkeuksellisen suuri. Sisäinen kitka perustuu kumimateriaalin korkeaan häviömoduliin ja erityisen matalaan elastiseen moduliin. Kumin viskoelastiset ominaisuudet riippuvat lämpötilasta ja taajuudesta. Sisäisen kitkan lisäksi kumin liukukitka perustuu myös adheesiohäviöihin.

Liukuja-alusta systeemissä, jossa kumipala liukuu kovalla ja karhealla alustalla, alustan karheudesta kohdistuu aikariippuvia deformaatioita kumin pintaan, joista syntyy viskoelastisia energiahäviöitä kumissa, mikä aiheuttaa liukukitkaa. Kumin häiriötaajuus riippuu alustan pinnankarheudesta ja liukunopeudesta. Monien luonnollisten pintojen pinnankarheutta voidaan kuvata itseaffiinisen fraktaalisena. Itseaffiininen fraktaalikuvaus on hyödyllinen liukukitkamallille, sillä siinä voidaan huomioida suuri määrä eri karheuskokoluokkia, ja näiden vaikutusta kitkaan siten arvioida.

Tässä diplomityössä tutkittiin kokeellisesti ja laskennallisesti kumipalan ja asfaltin muodostaman liukuja-alusta systeemin liukukitkaa. Liukukitkakerroin mitattiin lämpötilan ja liukunopeuden funktiona tällaiselle systeemille kylmähuoneessa. Mitattava lämpötila-alue oli välillä -8°C ja +32°C ja mitattava liukunopeusalue välillä 1 mm/s ja 1 m/s. Lisäksi optisella profilometrillä määritetyt kokeelliset parametrit, jotka kuvaavat asfaltin pinnankarheutta, ja liukujana käytettävien kuminäytteiden valmistajan kokeellinen data näytteiden viskoelastisista ominaisuuksista liitettiin laskennalliseen malliin.

Työssä toteutettu liukukitkateoria on siten uusi, että se huomioi sisäisen kitkan synnyttämän äkillisen paikallisten lämpötilojen nousun vaikutuksen kumiliukujassa. Tämän vaikutuksen huomioiminen on erityisen tärkeää yli 1 cm/s liukunopeuksille, joilla kumin lämpötilannousu on merkittävää.

Toteutetun mallin havaittiin ennustavan liukukitkakertoimen kvalitatiivisesti oikein liukunopeuden funktiona +21°C ja +32°C lämpötiloissa tehtyihin mittauksiin verrattuna liukunopeuksille välillä 1 mm/s ja 1 m/s. Kuitenkin mallin ennuste on kvantitatiivisesti huono, ja mallin havaittiin ennustavan suurimman kitkatason monikertaiseksi. Selitykseksi mallin ja mittausten väliselle erolle ehdotettiin eroja kokeellisissa olosuhteissa, kuten ilmankosteudessa ja siitä seuraavassa pintojen vesikerroksessa, joita mallissa ei oteta huomioon. Lisäksi liian alhainen kitkataso, jonka malli ennustaa alle 1 cm/s liukunopeuksille, selitettiin sellaisilla energianhukkamekanismeilla, joita malli ei huomioi, kuten ohuen, suljetun kontaminaatiokerroksen murtumisella ja halkeamien syntymisellä rajapinnalla. Kun kumin paikallisten lämpötilojen nousu huomioidaan, häviötangentin havaittiin ennustavan kvalitatiivisesti liukukitkatason ainakin nopeuteen 1 m/s asti. Asfalttipinnan vahvistettiin olevan itseaffiinisen fraktaalinen pintaprofiilin mittauksella.

Päivämäärä:	24.10.2013	Kieli:	Englanti	Sivumäärä:	59 + 17
Avainsanat:	Kumi, liukukitka, pinnankarheus, itseaffiinisuus				

Preface

This Master's thesis was done in the Vehicle Engineering group in the Department of Engineering Design and Production of Aalto University. I want to express my gratitude to the staff of the group for this opportunity. I also want to thank my supervising Professor Adam Foster for his work. I am thankful to Senior laboratory manager Panu Sainio, who was always there to help me and who is always approachable, and to my instructor Dr Ari Tuononen, who has encouraged me to nurture my intrinsic motivation in addition to having instructed my thesis and helped me throughout the work. The positive attitude and support from Mr Yi Xiong and Ms Mona Mahboob Kanafi made my time at the Vehicle Engineering group a daily, pleasurable journey around the world. I express my gratitude to them for that and for their academic support. I am thankful to Mr Antti Lajunen for many interesting discussions and his support.

I acknowledge the contribution from Senior laboratory manager Panu Sainio in operating the climate chamber and the linear friction tester setup, from Ms Mona Mahboob Kanafi for carrying out the GFM measurements, from Mr Bram Hunnekens and Dr Bo Persson for useful email discussions, and from Dr Tatiana Minav for academic support and proof-reading the thesis. I also acknowledge the contribution from Nokian Tyres for providing the rubber samples and the DMA data.

I am thankful to all my friends and especially Mr Mikko Poutanen, whose encouragement and friendship has proved invaluable many times. I am thankful to my family for their continuous support and endless love, without which this would not have been possible. Above all, I am grateful to my beautiful girlfriend Ms Elina Nissilä, whose support is unparalleled.

Copenhagen, 24.10.2013

Jukka Kärkimaa

Contents

Nomenclature

Abbreviations

AFM	Atomic force microscopy
DMA	Dynamic mechanical analysis
MATLAB	MathWorks MATLAB R2012b numerical computing environment
PSD	Power spectral density
ShA	Unit of the Shore A hardness scale
SLS	Standard Linear Solid
WLF	Williams-Landel-Ferry equation

Symbols

A	Area of real contact	m^2
A_0	Nominal contact area	m^2
c	Specific heat capacity	J/kg·K
$C(q)$	Surface roughness power spectrum	-
D	Heat diffusivity	$1/m^2 \cdot s$
D_f	Surface fractal dimension	-
$E(\omega)$	Viscoelastic modulus of rubber	Pa
F_x	Longitudinal force	N
F_z	Vertical load	N
h	Local substrate height from the average surface plane	m
h_0	Root-mean-square roughness of a surface	m
H	Hurst exponent	-
q	Wavevector	1/m
$\dot{Q}(\mathbf{x}, t)$	Heat production per unit volume and time	W/m^3
T_0	Ambient temperature	°C
T_g	Glass transition temperature	°C
T_q	Flash temperature	°C
$U(r)$	Lennard-Jones potential	-
v	Sliding velocity	m/s
λ	Wavelength of surface roughness	-
ω	Frequency of deformation of rubber	Hz
ρ	Density	kg/m^3
μ	Coefficient of sliding friction	-
ξ	Magnification factor	-
ν	Poisson ratio	-
σ_0	Nominal contact pressure	Pa

List of Figures

List of Tables

To the memory of my grandfather

1 Introduction

Contact mechanics and the physics of friction are fundamental disciplines of the engineering sciences and of vast technological importance for the construction of safe and energy-saving designs. Friction has been studied for a long time and several empirical macroscale laws have been established centuries ago. These include Amonton's laws, which were first recorded in print during the late 17th century [1].

Amonton's first law states that the force of friction is directly proportional to the applied load, while Amonton's second law states that the force of friction is independent of the apparent area of contact. In addition to Amonton's laws, there is Coulomb's law stating that kinetic friction is independent of the sliding velocity. da Vinci was the first engineer who persistently and quantitatively formulated the laws of friction and also the first to introduce the term *coefficient of friction* and to experimentally determine its typical value of 0.25. We have Leonard Euler, who worked on the mathematical point of view of friction as well as the experimental, to thank for the symbol μ as the coefficient of friction.

After centuries of scientific study, even today, at the fundamental level, a rigorous explanation for friction is yet to come. Friction is, in itself, energy dissipation and the explanation then has to elucidate the mechanisms, in which such energy dissipation occurs. Furthermore, friction can be approached on many different length-scales. Energy dissipation has been recently studied in atomic-scale friction in [2]. In addition, the effect of surface roughness and temperature on dry sliding friction at the atomic scale has been studied in [3]. There are sophisticated atomic-scale theories of friction, which extend some macroscopic friction laws to the nanoscale, and in the future they may help design miniaturized devices with optimal mechanical performance [4].

In this work, the sliding friction of rubber is investigated using a multiscale surface roughness approach. In a slider-substrate system of a rubber block sliding on a hard rough substrate, the substrate asperities will exert time-dependent deformations on the rubber surface resulting in viscoelastic energy dissipation in the rubber, which gives a contribution to the sliding friction [5]. Already in 1963, the friction of rubber was attributed to adhesion and deformation losses, governed by the viscoelastic properties of rubber [6]. It was noted then that for sliding speeds lower than 3 cm/s, the friction coefficient can be described as a function of sliding speed and temperature using a single master curve and the glass transition temperature of the material to describe the viscoelastic properties of the rubber slider.

The limit on the sliding speed in the applicability of early rubber friction theories [6–8] was there to avoid the effects of rising temperature due to frictional heating. This was in lack of a theory to quantitatively predict the temperature field in the rubber for higher sliding speeds and thus the inability to account for the changing material properties and predict the friction coefficient for such higher sliding speeds. For many engineering applications, however, such higher sliding speeds are typical, such as for car tyres during braking, and a theory to describe the sliding friction during high speed sliding would be invaluable for the design of such applications.

To tackle this problem, a new rubber friction theory [5] was developed, which

incorporates the *flash temperature effect* - the abrupt rise of local temperatures in a rubber slider on a hard rough substrate. In this work, the new theory is implemented in MATLAB. In addition, experiments on such a rubber-substrate system are conducted in a climate chamber. The sliding friction exhibited by a tyre rubber slider on a road asphalt surface is measured as a function of temperature and sliding speed. Experimental parameters describing the rubber and the asphalt surface are measured and incorporated in the implementation of the rubber friction theory.

Finally, the main aim is to validate the theory through comparison with the experimental results. The theory only takes into account the viscoelastic energy dissipation due to deformation of the rubber material during sliding on the hard rough substrate. Thus, a further aim is to assess the extent to which this energy dissipation mechanism accounts for the sliding friction as a function of sliding speed and consider the effect of other dissipation mechanisms involving adhesion. The entanglement of fascinating molecular-level physics and chemistry, and the beauty and applicability of large-scale engineering applications makes rubber friction such a fruitful topic for study.

In a general context, rubber friction is also related to rolling resistance and the development of automotive tyres [9]. In the future, fuel efficiency of vehicles becomes increasingly important. It is intrinsic to increasing the driving range of electric cars and to lowering greenhouse gas emissions, for instance. In Europe, 18 % of the total CO_2 emission originates from road transport and for a typical passenger car, for example, rolling resistance accounts for approximately 20–30 % of the energy consumption [10]. Lowering rolling resistance can thus greatly contribute to reducing greenhouse gas emissions and a better understanding of rubber friction is also of great importance for the development of low rolling resistance tyres.

2 Theoretical background

This chapter introduces the contact mechanics theories relevant to existing rubber friction models. In addition, the viscoelastic properties of rubber are covered. These two entities can be combined to form a model for the energy dissipation in a rubber bulk sliding on a rough surface. A historical perspective and the development of existing rubber friction theories are covered.

2.1 Contact mechanics

The contact mechanics theories relevant for existing rubber friction models including the one used in the rubber friction model implemented in this work are introduced in this chapter. The Hertz and Greenwood-Williamson contact theories are covered first. Then a short theory of adhesion is presented. Finally, the theory of self-affine fractal surfaces to be used later in this work is presented.

2.1.1 Hertz and Greenwood-Williamson contact theories

The Hertzian contact mechanics theory describes elastic spherical bodies with perfectly smooth surfaces such that in the contact of two such spheres there is only a vertical pressure [11]. One can determine the deformation field in the solids by minimization the elastic deformation energy. Name the radius of one sphere R_1 and that of the other sphere R_2, then upon squeezing together of the two spheres by the force F, the radius r_0 of the circular contact region is given by

$$r_0 = \left(\frac{R_1 R_2}{R_1 + R_2}\right)^{1/3} \left(\frac{3F(1-\nu^2)}{4E}\right)^{1/3}, \tag{1}$$

where

$$\frac{1-\nu^2}{E} = \frac{1-\nu_1^2}{E_1} + \frac{1-\nu_2^2}{E_2}, \tag{2}$$

where E_1 and E_2 are the elastic moduli of the solids and ν_1 and ν_2 are the corresponding Poisson ratios. The Poisson ratio is the negative ratio of transverse to axial strain. When an object is squeezed axially to a contraction with an applied load, and in a response, extends perpendicular to the axial direction, the ratio of the extension to the contraction is the Poisson's ratio ν, which will prove essential to the treatment of rubber friction in this work. The distance s by which the two spherical bodies approach each other (distance between the center points of the bodies being $R_1 + R_2 - s$), is given by

$$s = \left(\frac{R_1 + R_2}{R_1 R_2}\right)^{1/3} \left(\frac{3F(1-\nu^2)}{4E}\right)^{2/3} \tag{3}$$

By equations (2) and (3) we get for the special case of a sphere of radius R in contact with a flat surface the area of contact [12]

$$\pi r_0^2 = \pi R s \tag{4}$$

and the squeezing force

$$F = \frac{4E}{3(1-\nu^2)} s^{3/2} R^{1/2} \tag{5}$$

The pressure distribution in the contact area depends on the distance r from the center of the circular contact area and is given by

$$\sigma(r) = \sigma_0 \left[1 - \left(\frac{r}{r_0} \right)^2 \right]^{1/2}, \tag{6}$$

where $\sigma_0 = F/\pi r_0^2$ is the average pressure.

The Hertzian multiasperity contact model is illustrated in Fig. 2.1a. The characteristics of the Hertzian model are that all the surface asperities are of equal size and height.

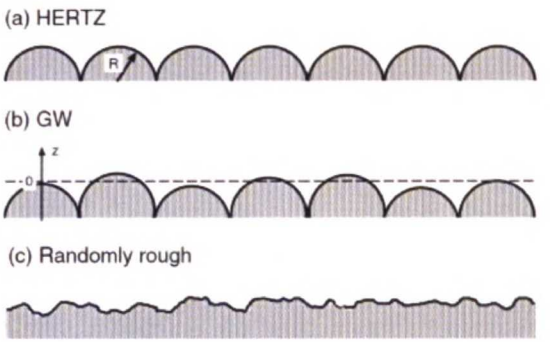

Figure 2.1: Three different models of rough surfaces: (a) Hertzian, (b) Greenwood-Williamson, (c) randomly rough. In (a) the asperities are of equal radius of curvature and equally high, whereas in (b) the height distribution is random. For (c), which is closest to real surfaces, both the height and the radius of curvature are distributed randomly. [13]

The Greenwood-Williamson model, on the other hand, is based on a random distribution of asperity heights [14], as illustrated in Fig. 2.1b. This difference is important, as for multiasperity contact models, the real area of contact and the load, as a function of the distance between the two approaching bodies, depends on the joint height distribution $P(h)$ [13]. In the Greenwood-Williamson model the height of the asperities is described with the following Gaussian height distribution

$$P_h = \frac{1}{(2\pi)(1/2)h^*} \exp\left(-\frac{h^2}{2h^{*2}} \right), \tag{7}$$

where h^* is the root-mean-square (RMS) amplitude of the asperity height fluctuation.

The difficulties of elastic contact theory arise because the displacement at any point in the contact surface is dependent on the distribution of pressure throughout the whole contact [15]. Therefore, an integral equation for the pressure is needed to find the pressure at any point in the contact. However, one can avoid these difficulties if the solids can be modelled by a simple Winkler elastic foundation instead of an elastic half-space. Such a foundation is illustrated in Fig. 2.2.

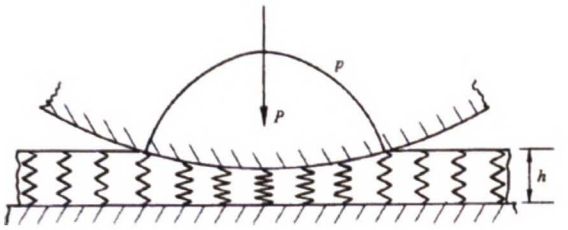

Figure 2.2: Illustration of a simple Winkler elastic foundation. [15]

The elastic foundation is of depth h, rests on a rigid base and is compressed by a rigid indenter. The indenter profile $z(x, y)$ is taken as the sum of the profiles of the two bodies being modelled

$$h(x) = h_1(x) + h_2(x) \tag{8}$$

The crucial property of the Winkler elastic foundation model is the one that there is no interaction between the springs of the model. The shear between adjacent elements of the foundation is thus ignored. The contact pressure at any point then depends only on the displacement at that point.

In the Greenwood-Williamson model then, with the above Winkler model and the Hertz contact theory with $s = h - d$ as the basis, the normalized area of real contact is given by [14]

$$\frac{\Delta A}{A_0} = \pi n_0 R \int_d^\infty \mathrm{d}h(h-d)P_h \tag{9}$$

A_0 denotes the nominal contact area whereas n_0 is the number of asperities per unit area. Calling the number of contacting asperities per unit area N we have

$$\frac{N}{A_0} = n_0 \int_d^\infty \mathrm{d}hP_h \tag{10}$$

and the nominal squeezing stress can be obtained as

$$\sigma_0 = \frac{F_N}{A_0} = \frac{4E}{3(1-\nu^2)} n_0 \int_d^\infty \mathrm{d}h(h-d)^{3/2} R^{1/2} P_h, \tag{11}$$

where F_N is the normal load. The Greenwood-Williamson theory can be extended to include adhesive contact between randomly rough surfaces, as well [14, 16].

It was found in 1957 by Archard, that for fractal-like surfaces the area of real contact is nearly proportional to the load [17]. Johnson et al. showed that the

area of contact between a rigid sphere and a flat rubber surface was larger than the value estimated from the Hertzian contact theory [18]. It was proposed that the molecular attraction of the van der Waals forces between the sphere and the rubber surface, lead to an increased contact area. Schallamach experimented on a rigid sphere sliding on a rubber surface and observed that true sliding in the form of slipping does not occur but instead folds are generated that are known as waves of detachment [19]. Today these waves of detachment are now known as Schallamach waves (see Section 2.3.2). In the next section, a short theory of adhesion involving the van der Waals attraction is presented.

2.1.2 Principles of adhesion

The origin of adhesion between neutral particles lies in intermolecular interactions called dispersion forces [20]. This interaction may be understood by considering an atom as a positively charged nucleus surrounded by a negatively charged electron cloud [21]. Although an atom or a molecule might not have a permanent dipole moment, it still has an instant dipole moment, which arises from the movements of the electron cloud. This dipole then induces dipole moments to the nearby atoms, which leads to attractive interaction between the atoms.

The attractive interaction can be described by the van der Waals potential, which decays as r^{-6} for interparticle separation r. If two atoms get too close, overlapping of the electron clouds leads to a repulsive interaction. With the semi-empirical twelfth-order term for repulsion, the interaction between two neutral atoms can be expressed as the Lennard-Jones potential [20]

$$U(r) = 4\epsilon \left[\left(\frac{\sigma}{r}\right)^{12} - \left(\frac{\sigma}{r}\right)^{6} \right], \tag{12}$$

where ϵ and σ determine the strength and the range of the interaction.

2.1.3 Self-affine fractal surfaces

As opposed to the Hertz and Greenwood-Williamson contact models, a real surface has roughness on multiple length scales. One way to describe a wide variety of real surfaces is a fractal treatment. Fractals are abundant and inherent to nature [22]. Intrinsic to the fractal treatment of surface roughness is that no length scale between the atomic and that clearly visible to the human eye is *a priori* discarded as unimportant.

Many natural surfaces can indeed be approximately described as self-affine surfaces over a rather wide roughness size region [23]. A self-affine fractal surface does not change its morphology, if we change the scale such that the change is appropriately different for the perpendicular direction as compared to the lateral directions. Hence, the statistical properties of the surface are invariant under the scaling transformation

$$x \to \zeta x, \quad y \to \zeta y, \quad z \to \zeta^H z, \tag{13}$$

where the Hurst exponent $0 < H < 1$, for surface fractal dimensions $2 < D_f < 3$.

Asphalt road and rubber are examples of surfaces that are self-affine fractal over a wide roughness size region. To characterize the surface roughness with respect to the length scales, surface roughness power spectrum $C(q)$ is defined by [24]

$$C(q) = \frac{1}{(2\pi)^2} \int d^2x \, \langle h(x)h(\mathbf{0}) \rangle \, e^{-iq \cdot x}, \tag{14}$$

where $x = (x, y)$ and $z = h(x)$ is the substrate height measured from the average surface plane, defined so that $\langle h \rangle = 0$. $\langle ... \rangle$ stands for ensemble averaging and q is the wavevector of surface roughness.

A characteristic surface roughness power spectrum is illustrated in Fig. 2.3. q represents the wavevector of surface roughness, q_L being the smallest possible wavevector, q_0 is the long distance wavevector and q_1 the short distance wavevector. The smallest possible wavevector q_L is obtained by [24]

$$q_L = \frac{2\pi}{L}, \tag{15}$$

where L is the linear size of the surface. In general, we obtain a wavevector by substituting the relevant lateral size for L in Eq. (15). The surface represented in the figure is self-affine fractal for $q_0 < q < q_1$.

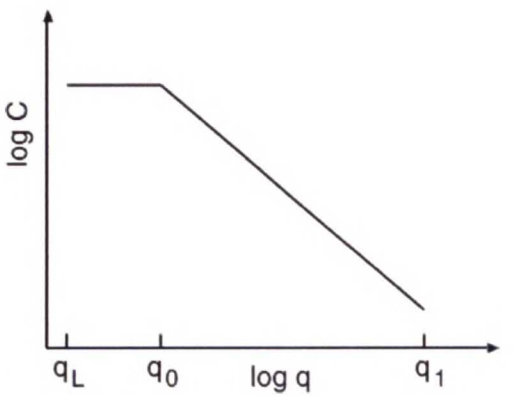

Figure 2.3: The surface roughness power spectrum of a surface, which is self-affine fractal for $q_0 < q < q_1$. C is the PSD and q the wavevector. q_L is the smallest possible wavevector, q_0 the long distance roll-off wavevector and q_1 the short distance cut-off wavevector. [24]

The slope of the curve k between q_0 and q_1 can be used to determine the surface fractal dimension D_f using equations (16) and (17) [12]

$$-2(H + 1) = k, \tag{16}$$

$$D_f = 3 - H, \tag{17}$$

where H is the Hurst exponent of the surface. For a self-affine surface, the power spectrum follows the power-law behaviour

$$C(q) \sim q^{-2(H+1)} \tag{18}$$

2.2 Viscoelastic properties of rubber

In this chapter, the most important viscoelastic properties of rubber in relation to the friction theory and the results presented later in this work are covered. The essential chemistry related to engineering viscoelasticity and some of the governing physical principles are presented. A basic rheological model, the time-temperature superposition and finally the effect of previous loading on the stress-strain response in a viscoelastic polymer material like rubber are covered. As an important aspect of the mechanical response of rubber, the focus is *linear viscoelasticity*. The theory presented in sections 2.2.1 – 2.2.4 is from [25], if not stated otherwise.

2.2.1 Theoretical overview

Because of its sensitivity to the chemistry and microstructure of the material, the *viscoelastic response* can be used as a probe in polymer science. Even though not all polymers are viscoelastic and even fewer are *linearly viscoelastic* [26], the following theory provides a useful engineering approximation and starting point in polymer and composites engineering. In linearly viscoelastic materials, there is a linear relationship between stress and strain at any given time [27].

Polymers may deform by either or both of two fundamentally different atomistic mechanisms upon the application of stress on them. The lengths and angles of the chemical bonds connecting the atoms may distort and the atoms move to new positions of greater internal energy, which corresponds to a very small motion with a related very small time scale, which is on the order of 10^{-12} s.

By combining the first and second laws of thermodynamics, one can derive the result of an increment of mechanical work $f\,dx$ done on the system as an increase in the internal energy dU or a decrease in the entropy dS

$$f\,dx = dU - T\,dS \tag{19}$$

As seen in Eq. (19), the relative importance of the entropic contribution is set by the temperature as the proportionality constant, and this provides a convenient means to experimentally determine whether the material's stiffness is energetic or entropic in origin. In contrast to the instantaneous nature of the energetically controlled elasticity, the conformational or entropic changes are processes whose rates are sensitive to the local molecular mobility. A variety of physical and chemical factors affect this mobility, including molecular architecture, temperature and the presence of absorbed fluids which may swell the polymer.

The rate of the above mentioned conformational changes can often be described to a reasonable accuracy by Arrhenius-type expressions of the form

$$\text{rate} \propto \exp\left(\frac{-E^{\dagger}}{RT}\right), \tag{20}$$

where $E^{\dagger}$ is an apparent activation energy of the process and $R = 8.314$ J/(mol·K) is the gas constant. A plot of rate versus temperature is presented in Fig. 2.4. For temperatures clearly above the *glass transition temperature* T_g, the rates are

virtually instantaneous, and the polymer acts in a rubbery manner. This means that the material exhibits large, instantaneous, and fully reversible strains in response to an applied stress.

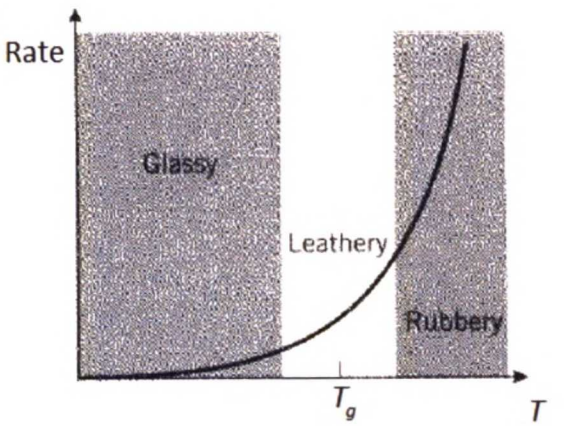

Figure 2.4: Temperature dependence of the rate of conformational changes. [25]

In contrast, at temperatures clearly below T_g, the rates of conformational or entropic change are so slow as to be negligible. This can be explained by the polymer chain uncoiling process being essentially "frozen out", so the polymer is able to respond only by bond stretching. Hence, it will respond in a glassy manner, that is instantaneously and reversibly but being incapable of being strained beyond a few percent before fracturing in a brittle manner.

Where the temperature is near T_g, the material will respond with a combination of viscous fluidity and elastic solidity, and this region is termed *leathery* or more technically *viscoelastic*, and also called the *transition region* [5]. An important descriptor of polymer thermomechanical response is the value of T_g, and it is also a fundamental measure of the material's propensity for mobility. Accordingly, factors that enhance mobility, such as absorbed diluents, expansive stress states, and lack of bulky molecular groups, all tend to produce lower values of T_g.

When the material is at a temperature well below T_g, such that entropic motions are frozen and only elastic bond deformations are possible, polymers exhibit a relatively high modulus, called the *glassy modulus* E_g on the order of 3 GPa. On the other hand, with a temperature increased through T_g, the stiffness drops dramatically, by perhaps two orders of magnitude, and the modulus is called the *rubbery modulus* E_r. In elastomers, which have been permanently crosslinked by sulphur vulcanization or other means, the value of E_r is determined primarily by the crosslink density. The kinetic theory of rubber elasticity gives

$$\sigma = NRT\left(\lambda - \frac{1}{\lambda^2}\right), \tag{21}$$

where σ is the stress, N is the crosslink density ($\mathrm{mol/m^3}$), and $\lambda = L/L_0$ is the extension ratio. Differentiation of equation (21) gives the slope of the stress-strain

curve at the origin as $E_r = 3NRT$. Ultimately, the plot of modulus versus temperature, such as the one shown in Fig. 2.5, is a vital tool in polymer materials science and engineering as it not only provides a map of a vital engineering property but is also a fingerprint of the molecular motions available to the material.

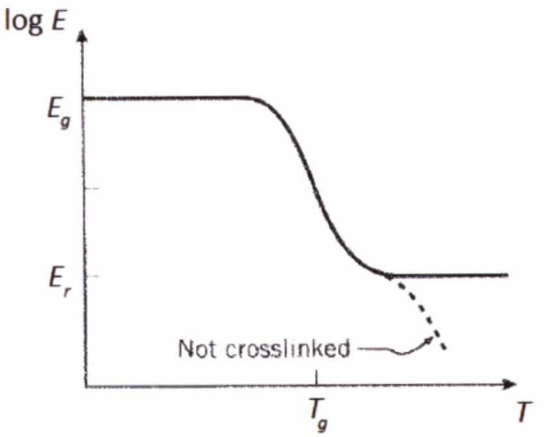

Figure 2.5: Temperature dependence of the modulus for polymers. [25]

2.2.2 Empirical quantities

To characterize viscoelastic materials experimentally in a laboratory in order to study the effect of the material structure and to obtain relevant information for actual in-use conditions, mechanical characterization in the form of uniaxial tensile tests with observation of the time dependency of the material response can be done. The most common such tests are creep test, stress relaxation test and dynamic loading.

The creep test consists of measuring the time dependent strain $\epsilon(t) = \delta(t)/L_0$, which results from the application of a steady uniaxial stress σ_0. Example results of a creep test are illustrated in Fig. 2.6.

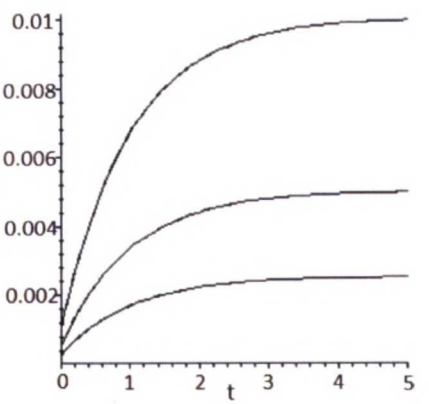

Figure 2.6: Creep strain at different constant stresses. [25]

With linear materials, the family of strain histories $\epsilon(t)$, which are obtained at various constant stresses may be superimposed by normalizing them based on the applied stress and the ratio of strain to stress is then called the *compliance* C. In the case of a time-varying strain arising from a constant stress, the ratio is termed the *creep compliance* and defined as

$$C_{crp}(t) = \frac{\epsilon(t)}{\sigma_0} \tag{22}$$

A typical form of this creep compliance function is presented in Fig. 2.7 as plotted against the logarithm of time.

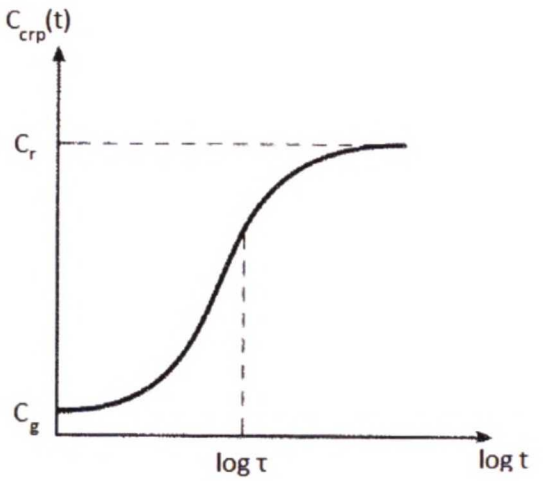

Figure 2.7: Creep compliance function. [25]

The second form to experimentally test viscoelasticity is the stress relaxation test. In this test one monitors the time-dependent stress resulting from a steady strain. Example curves of the relaxation response are presented in Fig. 2.8. As opposed to Fig. 2.6, in the stress test one measures the relaxation response to various levels of constant strain.

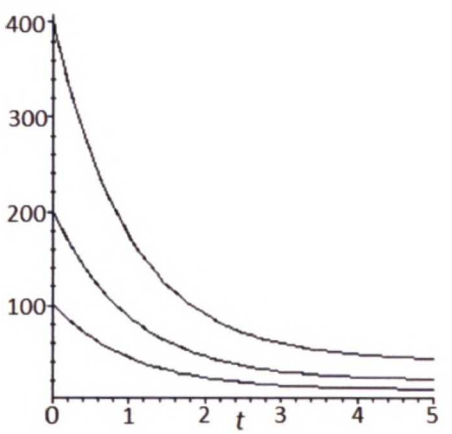

Figure 2.8: The relaxation response to three different levels of constant strain. [25]

Analogously to creep compliance, the relaxation curves can be superimposed by means of the *relaxation modulus* $E_{rel}(t) = \sigma(t)/\epsilon_0$, which has been plotted against the logarithm of time in Fig. 2.9.

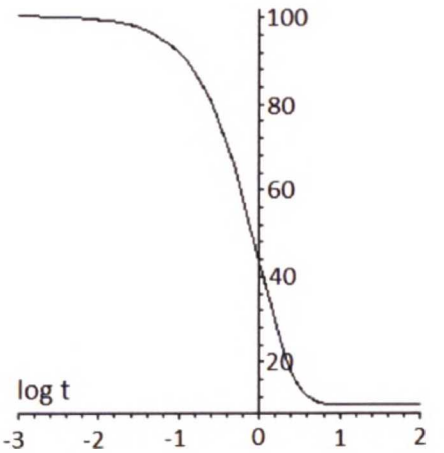

Figure 2.9: The stress relaxation modulus $E_{rel}(t)$ with $E_g = 100$, $E_r = 10$, $\tau = 1$. [25]

As seen in Fig. 2.9, at short time, the stress is at a high plateau, which corresponds to a *glassy* modulus E_g, and then falls exponentially to a lower equilibrium *rubbery* modulus E_r as the polymer molecules gradually accommodate the strain by conformational extension rather than bond distortion.

The similarity between creep and relaxation is that both are manifestations of the same molecular mechanisms, and thus it is intuitive to expect E_{rel} and C_{crp} to be related. The intuition may mislead one, however, because even though $E_g = 1/C_g$ and $E_r = 1/C_r$, in general $E_{rel}(t) \neq 1/C_{crp}(t)$. The relaxation response tends to move toward its equilibrium value more quickly than does the creep response.

The third and most important aspect of the experimental tests for characterization of viscoelastic materials with respect to this work is *dynamic loading*. This is because creep and stress relation tests are most suitable for studying material response at long times on the order of minutes to days, but dynamic loading is well-suited for filling out the short-time range of polymer response. In a dynamical loading test, one subjects the material to a sinusoidal strain or stress and measures the resulting stress or strain, respectively.

2.2.3 Steady-state modulus

When a viscoelastic material is subjected to a sinusoidally varying stress, a steady state will eventually be reached, the transient time also depending on the viscoelastic response time of the material. In such a steady state, the resulting strain will also be sinusoidal with the same angular frequency but retarded in phase by an angle δ. That the strain lags the stress by the phase angle δ is also true even if the strain rather than the stress is the controlled variable.

The stress and strain functions can be written as follows.

$$\epsilon = \epsilon_0 \cos \omega t, \tag{23}$$

$$\sigma = \sigma_0 \cos (\omega t + \delta) \tag{24}$$

Complex algebra can be exploited, as is typical in harmonic systems, and the stress function can be written as a complex quantity σ^* whose real part is in phase with the strain and whose imaginary part is 90° out of phase with it, as in Eq. (25).

$$\sigma^* = \sigma_0' \cos \omega t + i\, \sigma_0'' \sin \omega t \tag{25}$$

Here a complex quantity is denoted with the asterix and $i = \sqrt{-1}$ conventionally.

A visual representation of the observable stress and strain as a projection on the real axis of vectors rotating in the complex plane at a frequency ω is shown in Fig. 2.10.

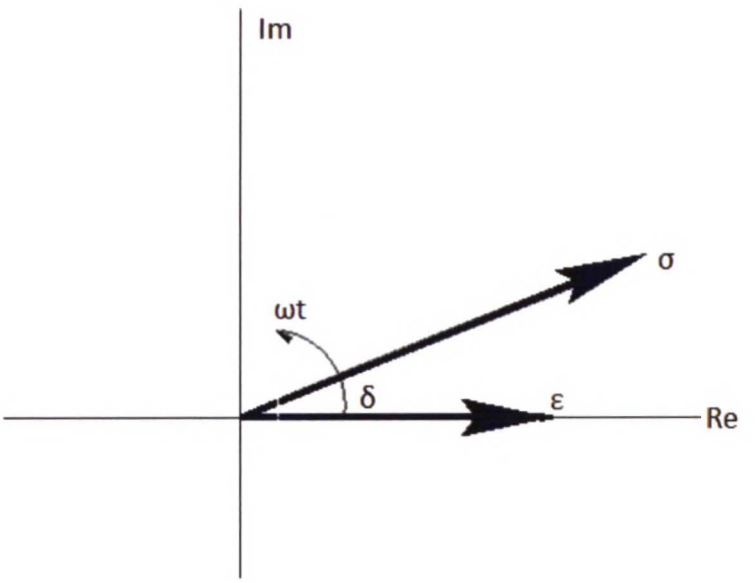

Figure 2.10: A presentation of harmonic stress and strain on the complex plain. [25]

As seen in the above figure, when the strain vector just passes the real axis, the stress vector will be ahead of it by the phase angle δ. Using the figure, the relations between the various parameters in harmonic relations can be derived as

$$\tan \delta = \sigma_0'' \,/\, \sigma_0', \tag{26}$$

$$|\sigma^*| = \sigma_0 = \sqrt{(\sigma_0')^2 + (\sigma_0'')^2}, \tag{27}$$

$$\sigma_0' = \sigma_0 \cos \delta, \tag{28}$$

$$\sigma_0'' = \sigma_0 \sin\delta \tag{29}$$

Using this complex form of the stress function, we define two different dynamic moduli. Both moduli are ratios of stress to strain but have very different molecular interpretations and macroscopic effects. The *real modulus* or *storage modulus* is defined as the ratio of the in-phase stress to the strain

$$E' = \sigma_0' \,/\, \epsilon_0 \tag{30}$$

The *imaginary modulus* or *loss modulus* is then defined as the ratio of the out-of-phase stress to the strain

$$E'' = \sigma_0'' \,/\, \epsilon_0 \tag{31}$$

Furthermore, it is convenient to write the harmonic stress and strain functions as exponentials

$$\sigma = \sigma_0^* e^{i\omega t}, \tag{32}$$

$$\epsilon = \epsilon_0^* e^{i\omega t} \tag{33}$$

The complex modulus can now be written as

$$E^* = \sigma_0^* \,/\, \epsilon_0^* \tag{34}$$

2.2.4 Time-temperature shift

As noted above, temperature has a dramatic effect on the viscoelastic response, and thus adjusting viscoelastic analysis for varying temperature is often necessary. For "thermorheologically simple" materials, the effect of changing the temperature is simply to shift the viscoelastic response without a change in the shape. This would correspond to changing the relaxation time τ without changing the glassy or rubbery moduli or compliances. A *time-temperature shift factor* $a_T(T)$ can be defined as the horizontal shift that must be applied to a response curve, such as $C_{crp}(t)$, measured at an arbitrary temperature T in order to move it to the curve measured at some reference temperature T_{ref}.

$$\log a_T = \log \tau(T) - \log \tau(T_{ref}) \tag{35}$$

The shift is illustrated in Fig. 2.11. Such a shift assumes a single relaxation time so that a single shift factor is applicable.

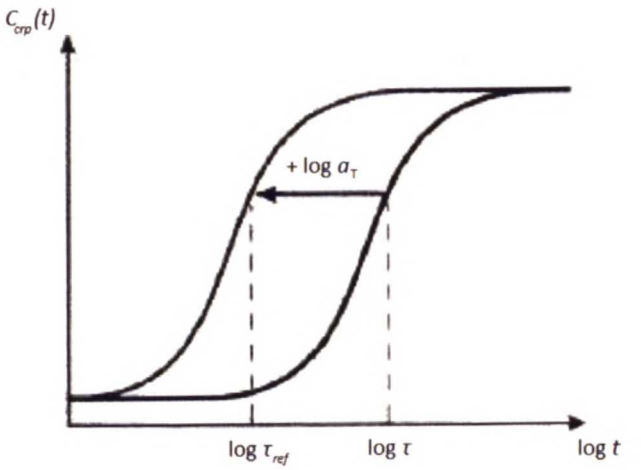

Figure 2.11: Illustration of the time-temperature shift factor a_T. [25]

The Williams-Landel-Ferry equation (WLF) is an empirical equation associated with time-temperature superposition. It was developed empirically [28] but rationalized in terms of free-volume concepts. The WLF equation has the form

$$\log a_T = \frac{-C_1(T - T_{ref})}{C_2 + (T - T_{ref})}, \tag{36}$$

where C_1 and C_2 are arbitrary material constants whose values depend on the material and choice of reference temperature T_{ref}. If T_{ref} is chosen to be T_g, then C_1 and C_2 often assume "universal" values applicable to a wide range of polymers, which is also an empirical finding

$$\log a_T = \frac{-17.4(T - T_{ref})}{51.6 + (T - T_{ref})}, \tag{37}$$

where T is in Celcius.

To apply WLF in order to predict the viscoelastic modulus E of rubber for changing temperatures, in accordance with [23], we will use in this work

$$E(\omega, T) = E(\omega a_T / a_{T_0}, T_0), \tag{38}$$

with

$$log_{10}\, a_T \approx -8.86 \frac{T - T_g - 50}{51.5 + T - T_g} \tag{39}$$

2.2.5 Rheological model

To predict the behaviour of the complex elastic modulus E of rubber as a function of frequency, we can use a rheological model such as the one depicted in Fig. 2.12.

E_1 is the storage modulus, E_2 is the loss modulus and τ is the characteristic time related to the damper. The elastic modulus for this model is given by

$$E(\omega) = \frac{E_1(1 - i\omega\tau)}{1 + a - i\omega\tau)}, \tag{40}$$

where ω is the excitation frequency of the rubber and we use the parameter values $E_1 = 10^9$ Pa, $a = 1000$ and $\tau = 10^{-3}$ s.

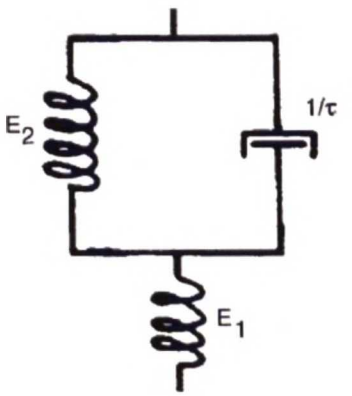

Figure 2.12: A rheological model. [8]

The model in Fig. 2.12, called the Standard Linear Solid model, is a poor description of real rubbers, as it predicts too abrupt a transition from the rubbery region to the glassy region with increasing frequency [23]. This will result in a too narrow and high $\mu(v)$ peak. Nevertheless, it gives a qualitatively correct $E(\omega)$.

2.2.6 Effect of previous maximum load

The Mullins' effect is a particular aspect of the mechanical response in filled rubbers. In essence, the stress-strain curve depends on the maximum loading previously encountered [29]. Although discovered 40 years ago, the Mullins' effect remains a major challenge in order to provide good mechanical modeling of the complex behaviour of industrial rubber [30]. No agreement has been found on the physical source of the effect either.

Several physical interpretations have been proposed, including chain breakage at the interface between the rubber and the fillers, slipping of molecules, rupture of the clusters of fillers, chain disentanglements and more complex composite structure formation. Such physical interpretations provide a basis for the emergence of physically motivated mechanical models.

When a new rubber material has been manufactured, it will effectively exhibit an appreciable change in its mechanical properties during the first extension. This effect is experimentally well-known in car tyres, for instance, as part of the *run-in effect*. When cyclically exerting a constant load on the new rubber material, it is typical to the Mullins' effect that most of the softening happens during the first loading cycle of the rubber. However, it takes a number of repeated loading cycles,

before the mechanical response of the rubber starts to coincide with the previous response. After that the softening that occured appears for loads lower or equal to the maximum load ever applied.

2.3 Rubber friction models

Modern rubber friction theories have developed since the 1960s. Two different approaches based on deformation losses in the bulk, and breaking and re-making of bonds were presented by Grosch and Schallamach in the same year 1963. Both theories produced similar results. In 2000 and 2001, more elaborated theories were presented by Heinrich and Klüppel, and Persson, respectively. All the theories assume low enough sliding speeds and neglect the effect of rising local temperatures in the rubber bulk due to frictional heating.

2.3.1 Grosch

Rubber friction was attributed to adhesion and deformation losses, governed by the visco-elastic properties of the rubber, in a study by Grosch in 1963 [6]. Grosch kept the highest sliding velocity below 3 cm/s in his experiments in order to avoid the effects of rising temperature due to frictional heating. It is noted in the study that, within this limited sliding velocity range, the friction coefficient can be described as a function of sliding speed and temperature using a single master curve and the glass transition temperature of the material. This can be done using the Williams, Landel, Ferry (WLF) tranform.

To test both friction mechanisms, adhesional and deformation friction, Grosch experiments on both smooth and rough surfaces. On smooth surfaces, the interfacial adhesion is assumed as the only source of friction, whereas with rough surfaces there is additionally the deformation of the rubber surface as the track asperities pass over it, that contributes to the friction. The master curve on a rough abrasive track shows, in general, two peaks, one of which is attributed to molecular adhesion and the other to the deformation.

The adhesion peak occurs at a relatively low velocity, which corresponds to the single peak on a smooth surface, whereas the deformation peak occurs at a considerably higher frequency, which reflects the frequency with which the track asperities deform the rubber surface. The deformation peak is absent on a smooth surface and the adhesion peak disappears with the introduction of a fine powder into the interface between the rubber and the track. Thus, it is concluded in the study that friction arises from adhesion and deformation losses, and that both are directly related to the visco-elastic properties of the rubber.

Furthermore, it is shown in Grosch's work that the coefficient of friction as a function of the sliding speed has a maximum and its position depends on the nature of the track. For the smooth surface, the maximum is very nearly symmetrical and the velocity, at which the maximum occurs, is proportional to the frequency at which the *loss modulus* (see Eq. (31)) is a maximum. On a rough surface, the curves are asymmetrical and the velocity of maximum friction is proportional to the frequency of maximum *loss tangent* (see Eq. (26)).

2.3.2 Schallamach

Also in 1963 a study on dynamic rubber friction by Schallamach was published [31]. In his approach, Schallamach assumes dynamic friction to arise from the shearing and subsequent breaking of distinct bonds between the rubbing members, and thus attributes friction to breaking and re-making of bond, which are due to local molecular adhesion between rubber and the track. Both formation and breaking of the bonds are described as thermally activated processes.

Developing this idea, Schallamach derives an equation for the frictional force F as

$$F = N_0 M V \tau \frac{(\bar{t}/\tau)^2}{1 + \bar{t}/\tau}, \tag{41}$$

where N_0 is the number of available sites, M is a force constant, V is the sliding velocity, τ is the average time between the breaking of a bond at a given site on one of the rubbing surfaces and the re-formation of a bond there, and $\bar{t}$ is the average life of the bonds. Schallamach's theory reproduces Grosch's experimental results in that the coefficient of friction as a function of the sliding velocity has a pronounced maximum.

In 1971 Schallamach presented a theory of *waves of detachment* [19], today known as *Schallamach waves*, for the sliding of rubber. Based on visual observations of contact areas between soft rubber sliders and hard tracks, and between hard sliders and soft rubber tracks, Schallamach explains the relative motion between the two frictional members in terms of such waves of detachment, which are crossing the contact area at high velocity from front to rear. In this description, qualitatively confirmed by experiment, adhesion appears complete between the waves which are moving folds in the rubber surface. The waves are likely to be produced by buckling, which is attributed to tangential compressive stresses.

2.3.3 Heinrich and Klüppel

A new approach to rubber friction was published in 2000 by Heinrich and Klüppel [7]. According to their theory, the hysteresis friction coefficient μ_H for a cylindrical rubber block undergoing a one-dimensional deformation during sliding contact with velocity v on a rough surface under a contact pressure σ_0 is given by

$$\mu = \frac{1}{2(2\pi)^2} \frac{\langle z_p \rangle}{\sigma_0 v} \int_{\omega_{min}}^{\omega_{max}} \omega \cdot E''(\omega) \cdot S(\omega) \, \mathrm{d}\omega, \tag{42}$$

where $\langle z_p \rangle$ is the mean penetration depth of the rubber given by

$$\langle z_p \rangle \cong \pi \cdot \xi_{\parallel} \frac{\sigma_0}{E'(\omega_{min})}, \tag{43}$$

where $E'(\omega_{min})$ is the storage modulus corresponding to an excitation frequency related to the parallel correlation length $\xi_{\parallel}$ of the surface correlation function

$$\omega_{min} = \frac{2\pi v}{\xi_{\parallel}} \tag{44}$$

$E''(\omega)$ is the loss modulus of the bulk rubber and $S(\omega)$ is the power spectral density of the surface height profile, which, in case of a self-affine fractal surface such as an asphalt surface [32], can be calculated using a power law (see Section 2.1.3).

The Heinrich and Klüppel model can be used for numerically predicting the sliding friction coefficient as a function of sliding speed, contact pressure or temperature. With the introduction of an optimized free parameter as a factor of the friction coefficient, the model prediction matches experimental data well up to a sliding speed on the order of cm/s [33].

2.3.4 Persson

In 2001, Persson published a new approach to rubber friction [8]. This theory is similar to the Heinrich and Klüppel theory in that it predicts the friction experienced by a bulk rubber slider on a rough substrate based on the viscoelastic properties of the rubber and the statistical roughness of the substrate and the contact properties. The contact properties include the sliding speed, contact pressure and temperature. The main difference between the two friction models lies in the underlying contact mechanics theory.

While Heinrich and Klüppel built their friction model based on the one-dimensional Greenwood-Williamson theory of elastic contact (see Section 2.1.1), Persson's friction model is based on a three-dimensional contact mechanics theory. The Persson 2001 theory does not take into account the effect of adhesion, as the key result is, that for tread rubbers in contact with rough surfaces, the adhesive interaction is negligible and the sliding friction is dominated by the hysteresis friction given by

$$\mu = \int_{q_L}^{q_1} q^3 C(q) P(q)\,\mathrm{dq} \int_0^{2\pi} cos\,\phi\ \mathrm{Im}\frac{E(q\,v\,cos\,\phi)}{(1-\nu^2)\sigma_0}\,\mathrm{d}\phi, \tag{45}$$

where σ_0 is the macroscopic contact pressure, E is the complex viscoelastic modulus of the rubber slider and ν is Poisson's ratio of the rubber. q is the wavenumber related to the roughness wavelength λ via $q = 2\pi/\lambda$. $C(q)$ is the 2D PSD of the surface height profile, as in Eq. (14). The function $P(q)$ represents the real area of contact between the rubber and the rough surface. Via the funtion $P(q)$, the theory takes into account how the rubber is able to follow the hard substrate profile on each roughness level q, which is a major difference to the Heinrich and Klüppel theory. The Persson theory will be covered in more detail in the next section.

A systematic deviation between the Persson 2001 friction model prediction and experimental data has been reported for sliding speeds higher than the order of cm/s, whereas a very good match has been reported for lower sliding speeds [33]. The deviation is attributed to thermal effects, which are not taken into account in the theory, namely the local heating of the rubber due to friction.

The viscoelastic properties of rubber are strongly temperature dependent, and local heating effects in the rubber may be important for sliding speeds on the order of cm/s and higher [5]. Thus, it is necessary to include the local temperature increase in the friction model. Persson presented an extended theory incorporating the local

heating effect, so-called *flash temperature effect*, in 2006 [5]. This rubber friction model and its implementation will be covered in the next section.

3 Persson rubber friction model

The following treatment of rubber friction by Persson is based on the idea that a rubber block sliding on a hard rough substrate undergoes time-dependent deformations, excited by the substrate surface asperities. The deformations then result in viscoelastic energy dissipation in the rubber, which contributes to the sliding friction. In this work, only Persson's *stationary sliding* model [5] is covered, which means a constant sliding velocity v is assumed. Accordingly, μ is defined as the coefficient of *sliding friction*. This chapter is based on [5], if not stated otherwise.

Such a rubber block-substrate system is illustrated in Fig. 3.1. As the rubber block slides on the rough substrate, with surface roughness on multiple length scales, the larger surface asperities exert pulsating forces on the rubber block, which results in viscoelastic energy dissipation in the larger volume elements indicated using yellow dashed lines in Fig. 3.1. On top of the larger surface asperities there are smaller surface asperities, which again cause energy dissipation in the smaller volume elements indicated by the red dashed lines. The temperature thus builds up in the rubber and this so called *flash temperature effect* has to be incorporated in a full treatment of rubber friction.

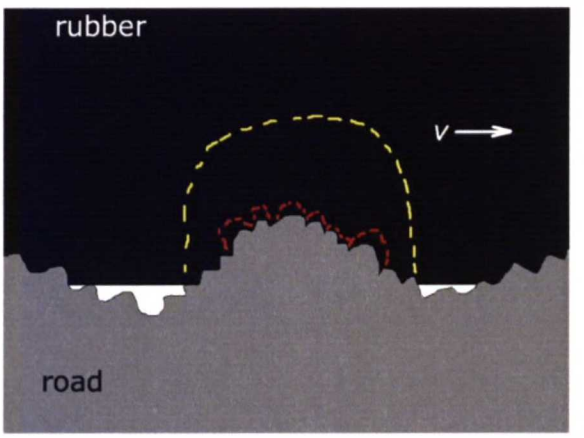

Figure 3.1: Illustration of a rubber block sliding on a hard rough substrate. The pulsating forces exerted by the road asperities on the sliding rubber block lead to energy dissipation in the rubber via the internal friction of the rubber. The dashed lines illustrate the volume elements inside which most of the energy dissipation occurs. The energy dissipation inside the larger volume elements (indicated in yellow) are induced by the larger road asperities and the smaller dissipative regions (indicated in red) result from the smaller asperities distributed on top of the larger asperities. Adapted from [5].

In what follows, the Persson rubber friction model is covered starting from his approach to surface roughness and the 2001 theory [8], which excludes the *flash temperature effect*. Then the 2006 theory [5], in which the *flash temperature effect* is incorporated, is covered. Finally, the structure of the implementation of the 2006 theory written in MATLAB for this work is presented.

3.1 Surface roughness theory

The surface roughness power spectrum $C(q)$, defined in Eq. 14, mainly determines the influence of surface roughness on rubber friction [5]. As explained in Section 2.1.3, many surfaces tend to be nearly self-affine fractal and for such surfaces the power spectrum has the power law behaviour of Eq. (18). Asphalt and concrete road pavements have almost perfect self-affine fractal power spectra, with a well-defined roll-off wavevector q_0, which is of order 1000 m^{-1} and corresponds to $\lambda_0 \approx 1$ cm, reflecting the largest stone particles used in the asphalt. In the following treatment of surface roughness, a self-affine fractal power spectra is assumed.

When an elastic solid with a flat surface is squeezed against a hard, randomly rough substrate, typically a partial contact will occur. How large the true contact area appears depends on the length scale at which we observe the contact. This is illustrated in Fig. 3.2, which features zooming factors of $\xi = 1, 10, 100$. The zooming factor refers to some arbitrarily chosen reference length scale, such as the lateral size L of the nominal contact area. For this work, we use the roll-off wavelength $\lambda_0 = 2\pi/q_0$ as the reference length. Then $\xi = \lambda_0/\lambda = q/q_0$, with λ being the shortest roughness wavelength, which can be resolved with the zooming factor ξ, and q the corresponding wavenumber. With $\xi = 1$, the contact with the rubber at many *macro-asperities* of the rough surface appears complete, whereas with a greater zooming factor, those *macro-asperity* contacts break down into partial contacts between smaller, constituent asperities of the *macro-asperity* and the rubber.

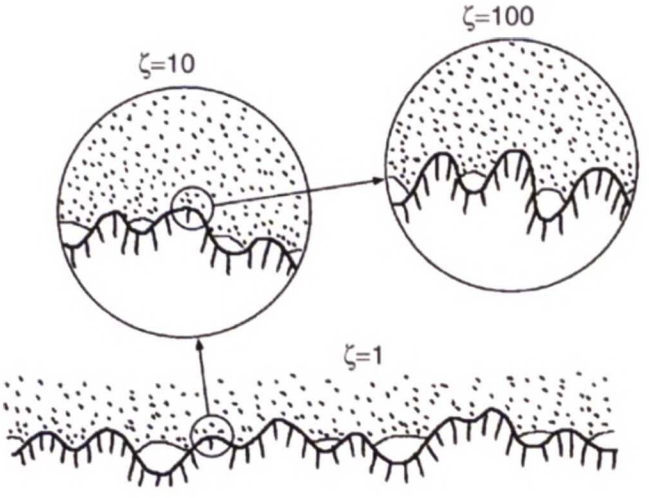

Figure 3.2: Illustration of a rubber block (dotted area) in adhesive contact with a hard rough substrate (dashed area). The substrate features roughness on multiple length scales and the rubber makes partial contact with the substrate on all length scales. When one assesses the contact area at low magnification ($\xi = 1$) it appears that complete contact occurs in the macro-asperity contact regions. In reality, however, only partial occurs. Increasing the magnification elucidates the partial contact. [5]

So, intuitively the contact diminishes with an increasing zooming factor. This

can also be seen in Fig. 3.3. However, there is a short distance cut-off, for which the minimum is an atomic distance. The short distance cut-off wavevector q_1 is illustrated for self-affine fractal surfaces in Fig. 2.3. For rubber friction, the effective short distance cut-off may be much larger, on the order of 1 μm.

The concept of *macro-asperity* contact area is intrinsic to the rubber friction model to be presented. For a self-affine fractal surface, with a roll-off wavevector q_0 corresponding to magnification $\xi = 1$, the macro-asperity contact is defined as the contact region between the solids when the system is studied at a low magnification $\xi = \xi_m \approx 2$–5. This is illustrated in Fig. 3.3, which shows the result of a molecular dynamics calculation. The average size of a macro-asperity contact region is discussed in Appendix A of [5].

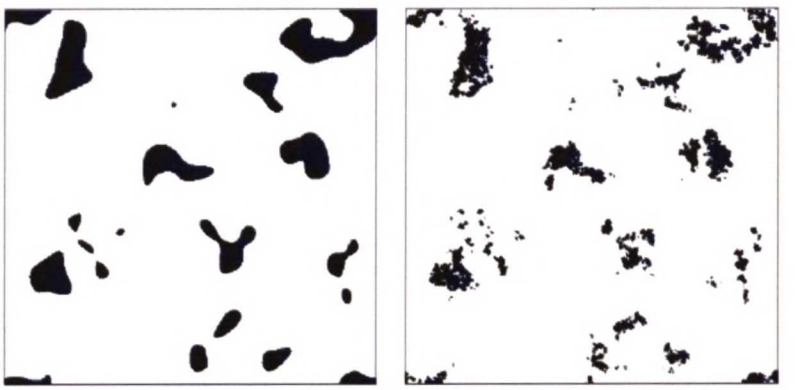

Figure 3.3: Illustration of macro-asperities at the contact area between an elastic solid with a flat surface and a hard randomly rough substrate. The picture on the left illustrates a magnification $\xi = 4$ and the picture on the right has $\xi = 216$. The surface has the fractal dimension $D_f = 2.2$ and $q_0/q_L = 3$. [34]

If we consider the contact between two solids at a low nominal contact pressure $\sigma_0 = F_N/A_0$, such that the contact area is proportional to the load, and observe the contact at the length scale λ_0/ξ_m, then the solids will make apparent contact at a low concentration of widely separated contact areas. Since the separation between the macro-asperity contact regions is very large, the interaction between the macro-contact regions is neglected. Then the pressure in the macro-asperity contact regions will be of order $q_0 h_0 E$, with h_0 being the rms roughness amplitude and E the elastic modulus. The average pressure in the macro-asperity contact regions is thus independent of the nominal contact pressure σ_0.

The smaller micro-asperities on top of the macro-asperities, on the other hand, will be close enough to each other at a small enough length scale, and therefore the elastic and thermal interaction between the micro-asperities cannot be neglected in a rigorous treatment of rubber friction. This fact will be accounted for in the hot friction theory presented in Section 3.3.

3.2 Cold friction theory

Neglecting the flash temperature effect, i.e. the thermal coupling between the micro-asperities, the sliding friction coefficient at velocity v is determined by [8]

$$\mu = \frac{1}{2}\int_{q_L}^{q_1} q^3\, C(q)\, P(q)\, \mathrm{d}q \int_0^{2\pi} cos\,\phi\ \mathrm{Im}\frac{E(q\,v\,cos\,\phi)}{(1-\nu^2)\sigma_0}\,\mathrm{d}\phi, \tag{46}$$

where

$$P(q) = \mathrm{erf}\left(\frac{1}{2\sqrt{G}}\right), \tag{47}$$

with

$$G(q) = \frac{1}{8}\int_{q_L}^{q} q^3\, C(q)\, \mathrm{d}q \int_0^{2\pi} \left|\frac{E(q\,v\,cos\,\phi)}{(1-\nu^2)\sigma_0}\right|^2 \mathrm{d}\phi, \tag{48}$$

where σ_0 is the macroscopic contact pressure, E is the complex viscoelastic modulus of the rubber slider and ν is Poisson's ratio of the rubber, which typically equals 0.5. The function $P(q)$ represents the real area of contact between the rubber and the rough surface and is defined as

$$P(\lambda) = \frac{A(\lambda)}{A(L)}, \tag{49}$$

where L is the diameter of the macroscopic contact area and λ is the length scale at which the contact problem is analyzed. The results then only depend on viscoelastic modulus $E(\omega)$ of the rubber, and on the substrate surface roughness power spectrum $C(q)$. The frequency of the pulsating forces on the rubber excited by the substrate is defined as $\omega = q\,v\,cos\,\phi$. The angle ϕ denotes the direction of a single constituent cosine roughness profile of the rough surface, illustrated in Fig. 3.4. Only if the roughness profile has a component with the wavevector along the sliding direction v, will there be pulsating forces on the rubber.

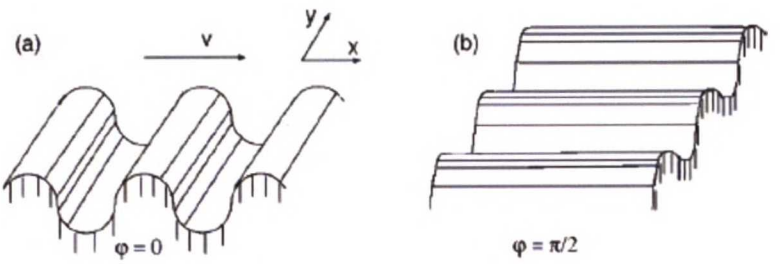

Figure 3.4: Illustration of a cosine roughness profile with the wave vector (a) along, and (b) perpendicular to the sliding direction. [8]

In accordance with the above equations, the theory takes into account the substrate surface components with wavevectors in the range $q_L < q < q_1$, with q_L being the smallest relevant wavevector, and in case of a rubber slider, L is the lateral size of the slider. As q_L for a tyre tread block is smaller than the roll-off wavevector q_0 of the power spectra of most road surfaces, rubber friction is very insensitive to the

exact value of q_L. q_1, on the other hand, may have different origins, like real road contamination, for instance.

We note that, in accordance with the viscoelasticity theory in Section 2.2, the friction coefficient μ depends directly on the *loss modulus* $\mathrm{Im}(E)$ and the real area of contact P depends both on the *storage modulus* and on the *loss modulus*, i.e. the magnitude of the complex viscoelastic modulus $|E|$.

3.3 Hot friction theory

For this theory, thermal coupling between the macro-asperity contact regions will be neglected. This should be a good approximation as long as the contact area at the magnification ξ_m is much smaller than the nominal contact area, which implies that the distance between the macro-asperity contact regions is much larger than the linear size of these regions, which is of order λ_0/ξ_m.

The temperature field $T(\mathbf{x}, t)$ inside a sliding rubber block is determined by

$$\frac{\partial T}{\partial t} - D\nabla^2 T = \frac{\dot{Q}(\mathbf{x}, t)}{\rho C_V}, \tag{50}$$

where $\dot{Q}$ is the energy production per unit volume and unit time resulting from the internal friction of the rubber. The heat diffusivity is $D = \lambda/\rho C_V$, with ρ being the mass density, λ the heat conductivity and C_V the heat capacity. The typical values for rubber are $\rho \approx 10^3$ kg/m^3, $C_V \approx 10^3$ J/kg·K and $\lambda \approx 0.1$ W/m·K, which results in $D \approx 10^{-7}$m^2/s. The temperature rise in the rubber on top of a single substrate asperity is illustrated in Fig. 3.5.

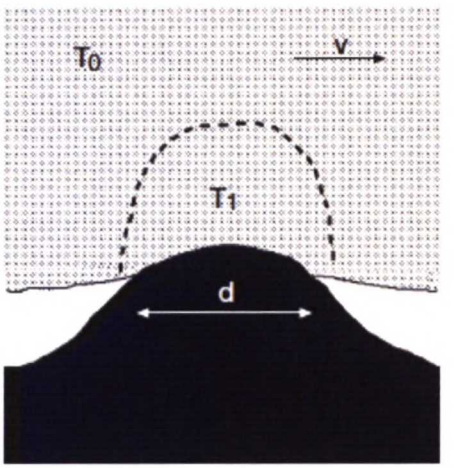

Figure 3.5: Illustration of the temperature rise in a sliding rubber block. The heat production $\dot{Q}(\mathbf{x}, t)$ per unit volume and unit time occurs mainly within the volume element on top of a substrate asperity indicated by the dashed line, with temperature $\mathrm{T}_1 > \mathrm{T}_0$. [5]

An asperity contact area with diameter d, like in the above figure, will generate pulsating forces on the rubber with frequency $\omega_0 \approx v/d$ resulting in energy dissipa-

tion in a volume element of order d^3. With a high enough sliding velocity v, the heat diffusion during the time period d/v will be negligible and the temperature increase in the rubber around the asperity will be $\Delta T \approx Q/\rho C_V$, with Q being the frictional heat energy per unit volume in the volume element d^3. For such negligible heat diffusion the effective contact time d/v has to be smaller than the diffusion time d^2/D, implying $vd > D$. Then for instance with $v = 0.1m/s$, heat diffusion can be neglected if $d > D/v \approx 10^{-6}m$. However, the peak temperature will decrease after the contact in a way determined by the heat diffusion equation.

Consider an idealized case where surface roughness occurs with randomness on a single length scale $\lambda_0 = 2\pi/q_0$ with the root-mean-square roughness amplitude h_0. The surface roughness power spectrum is $C(q) = (h_0^2/2\pi q_0)\delta(q - q_0)$ and the average radius of curvature of the asperities is $R \approx 1/(q_0^2 h_0)$. Referring to Fig. 3.5, it is assumed that no roughness occurs on a smaller length scale than the size of the asperity d. The heat energy produced in the volume element d^3 at the asperity during the effective contact time d/v is given by $\mu F_N d$, with $F_N = \sigma d^2$ the normal asperity load, where σ is the average perpendicular stress in the contact area. The energy production per unit volume is then $Q \approx \mu F_N d/d^3 = \mu\sigma$. The temperature increase, neglecting the heat diffusion, is given by $\Delta T \approx Q/\rho C_V \approx \mu\sigma/\rho C_V$. By [35], the friction coefficient will be

$$\mu \approx \sigma \frac{\operatorname{Im} E(\omega_0, T)}{|E(\omega_0, T)|^2}, \tag{51}$$

with $\omega_0 = vq_0$. From standard contact mechanics we have $\sigma \approx q_0 h_0 |E(\omega_0, T)|$, which yields

$$\mu \approx q_0 h_0 \frac{\operatorname{Im} E(\omega_0, T)}{|E(\omega_0, T)|}, \tag{52}$$

Thus the temperature will be

$$T \approx T_0 + (q_0 h_0)^2 \frac{\operatorname{Im} E(\omega_0, T)}{\rho C_V}, \tag{53}$$

where T_0 is the background temperature. As the complex viscoelastic modulus $E(\omega, T)$ depends on the local temperature T, we use the Williams-Landel-Ferry equation (WLF) to approximately describe the temperature dependence as in equations (38) and (39). These equations to describe the temperature dependence in combination with equations (52) and (53) form a complete set of equations from which the temperature T and the friction coefficient μ can be obtained.

Figure 3.6 illustrates the situation with a randomly rough substrate, in which there are asperities of smaller roughness size d_2 on top of the larger asperity of size d_1 with corresponding local temperatures $T_2 > T_1 > T_0$ in the rubber block surface sliding on top of the substrate. T_0 is the background temperature and the asperity temperatures are $T_1 = T_0 + \Delta T_1$ and $T_2 = T_1 + \Delta T_2$. The temperature will then effectively increase, when we go to smaller and smaller asperity contact regions. In this case there will be thermal overlap between the heat produced in

the micro-asperity contact area inside every macro-asperity contact area, meaning the temperature rise at one micro-asperity contact area will produce a subsequent temperature rise at a neighbouring micro-contact. To incorporate this, Persson uses a mean field type of approximation where the heat sources associated with the micro-asperity contacts are smeared out laterally within a macro-asperity contact.

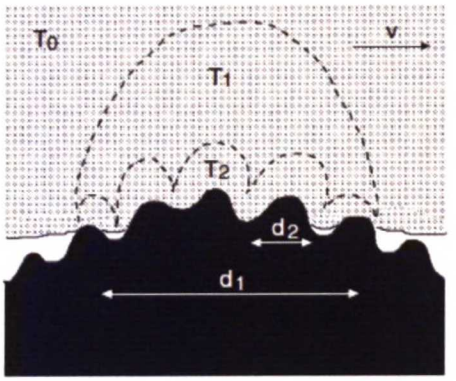

Figure 3.6: Illustration of the temperature build-up in a sliding rubber block on a randomly rough substrate. [5]

Finally, for the implementation of the friction model for a randomly rough substrate with the *flash temperature* T_q for each roughness wavenumber q, we need to solve equations (54) – (56) for T_q. For a rigorous derivation of the equations, see [5].

$$f(q) = \frac{vq^4}{\rho C_V} C(q) \frac{P(q)}{P(q_m)} \int_0^{2\pi} \cos\phi \, \mathrm{Im} \frac{E(q\, v \cos\phi,\, T_q)}{1-\nu^2} \, \mathrm{d}\phi, \tag{54}$$

$$g(q,q') = \frac{1}{\pi} \int_0^{\infty} \frac{1}{Dk^2} \left(1 - e^{-Dk^2 t_0}\right) \frac{4q'}{k^2 + 4q'^2} \frac{4q^2}{k^2 + 4q^2} \, \mathrm{d}k, \tag{55}$$

where $t_0 \approx R/v$ is approximately half the time a rubber patch is in contact with a macro-asperity. For an estimation of the radius R of a macro-asperity contact region, we again refer to Appendix A of [5].

$$T_q = T_0 + \int_0^{\infty} g(q,q') f(q') \, \mathrm{d}q' \tag{56}$$

Once we have obtained T_q for all q, the friction coefficient can be calculated using the equations from cold friction theory and incorporating the temperature dependency of the viscoelastic modulus E

$$\mu \approx \frac{1}{2} \int_{q_0}^{q_1} q^3 \, C(q) \, P(q) \, \mathrm{d}q \int_0^{2\pi} cos\,\phi \; \mathrm{Im} \frac{E(q\, v \cos\phi,\, T_q)}{(1-\nu^2)\sigma_0} \, \mathrm{d}\phi, \tag{57}$$

where

$$P(q) = \mathrm{erf}\left(\frac{1}{2\sqrt{G}}\right), \tag{58}$$

with

$$G(q) = \frac{1}{8} \int_{q_0}^{q} q^3 C(q)\, \mathrm{d}q \int_0^{2\pi} \left| \frac{E(q\, v \cos\phi,\, T_q)}{(1-\nu^2)\sigma_0} \right|^2 \mathrm{d}\phi \tag{59}$$

3.4 Implementation

This chapter introduces the structure of the implementation of the Persson hot friction theory written for this work. Computational performance and validity of the solution are considered. The solution was implemented using ideas from [36] for numerically solving for the flash temperature. The solution written in MATLAB is presented in Appendix A.

3.4.1 Structure of the solution

The viscoelastic modulus E can either be theoretically approximated using a rheological model, such as the SLS, or obtained using experimental data. For this work, DMA data was received from Nokian Tyres with the tyre rubber samples. Hence, the experimental data is incorporated in the solution. The model was also implemented with the SLS, as this allows for assessment of the solution with well-defined, functional data. To illustrate the general structure of the solution, a flow chart is presented in Fig. 3.7.

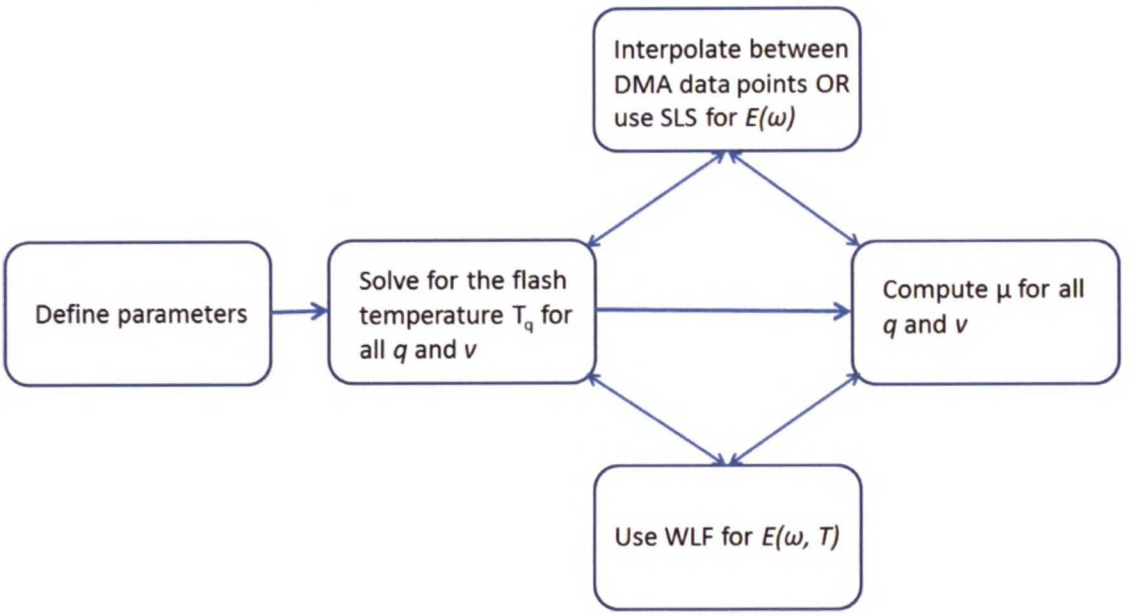

Figure 3.7: Flow chart for the implementation of the Persson hot friction theory.

As illustrated in Fig. 3.7, the model parameters are first defined. Then the flash temperature T_q is solved for all roughness sizes q and sliding speeds v. In computing the equations (54) and (59) involving the viscoelastic modulus $E(\omega)$, either DMA data or SLS model is used, as explained above. To evaluate $E(\omega, T)$, the WLF

equation is used. After solving for the flash temperatures, the friction coefficient μ is computed for all q and v, and again either DMA data or SLS model is used for $E(\omega)$ and WLF for $E(\omega, T)$, when evaluating Eq. (57).

A pseudocode of solving for the flash temperature is presented in Appendix B, with step-by-step references to the MATLAB files of the solution in Appendix A. Essential for the numerical solution is that the bisection method is used to iterate and find the flash temperature T_q for each roughness size q and sliding speed v, as equations (54) – (56) are implicit for variable T_q. An important aspect is that in computing the flash temperature, one iterates over all the roughness sizes q' using a constant temperature T_q as in Eq. (55). In other words, it is important to note that T_q is a function of q, not q'.

3.4.2 Improving performance

To improve the performance, code profiling was done. The most computationally intensive part of the implementation is solving for the flash temperature, because we are iterating in the bisection method and for each iteration we have to compute numerical integrals. The part which takes most of the computation time is the *P_numerical.m* as in Appendix A.4. This is because of the numerical integration with interpolation between the DMA data points. The run-time of the function would drop to about 1/20 by compiling the MATLAB function into a MEX-file, called *P_numerical_mex* in the code.

As we are interested in the sliding friction as a function of the sliding speed, the same equations for different values of the sliding speed v are computed. This is were we can parallelize. Thus a *parfor* loop is used in MATLAB in the *run_model.m* as in Appendix A.1 to compute the flash temperature over a range of values of v.

With these considerations the overall run-time for 15 different values of v was about 5 hours on a dual-core 1.8 GHz Intel Core i5. Thus the most modern multi-core CPUs or a cluster will allow for effective parameter sensitivity study with the implementation.

3.4.3 Verifying the solution

To verify the solution, results in [5] were compared to our own with the same parameters. As also noted in [36], the reason for differences between the Persson results and a custom solution of the theory may lie purely in the fact that Persson uses his own measurement data for the viscoelastic modulus and the shift factor a_T, which is not published.

However, using the Standard Linear Solid (SLS) model, similar qualitative behaviour was confirmed for the friction coefficient and the flash temperature as presented by Persson. In particular, the plot of the flash temperature against the sliding speed as in Fig. 11 of [5] and the plot of the flash temperature against the magnification factor as in Fig. 12 of the same publication are very similar in the shape.

The model predictions were also computed with experimental data of this work, as presented in Table 5.6, except that the SLS was used for the viscoelastic modulus

instead of the DMA data for assessment of the model. The results with the SLS model are presented in Appendix C. The behaviour of the sliding friction coefficient as a function of the sliding speed is similar to that of Fig. 11a of [5] for both the cold and hot friction models, which also suggests that the model has been correctly implemented, when using the SLS model.

4 Experimental methods

This chapter introduces the experimental methods used to gather data for studying rubber friction and comparing the model predictions to the experiments. The surface roughness of the asphalt was measured with an optical profilometer, the viscoelastic properties of the rubber samples using dynamic mechanical analysis and the hardness of the rubber samples with a durometer. Finally, the sliding friction was measured in a linear friction tester.

4.1 Profilometry

Portable optical profilometer from GFM was used to characterize the roughness of the asphalt surface used in the friction tests [37]. The device is shown in Fig 4.1. The device features a measuring area of 320 by 240 mm^2 with a lateral resolution of 200 μm and a height resolution of 20 μm. The data acquisition time is about 2 s, which allows for repeated measurements.

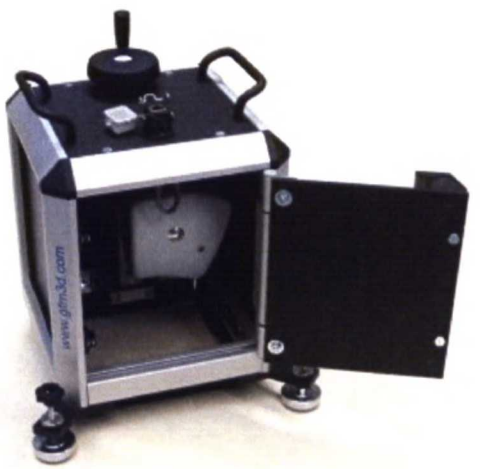

Figure 4.1: Photograph of the GFM apparatus. [37]

The device comes with a software package ODSCAD, which is used for data processing. The data was also further processed with MATLAB. The power spectral density (PSD) with the surface fractal dimension D_f, as well as the cut-off frequency q_1 are obtained from the data and can then be incorporated in the friction model. The 2D and 3D surface profile images can also be used for assessment of the surface wear.

4.2 Rheometry using dynamic mechanical analysis

Dynamic Mechanical Analysis (DMA) technique is widely used to characterize a material's properties as a function of temperature, time, frequency, stress, atmosphere or a combination of these parameters. In DMA, a small deformation is applied to

a sample in a cyclic manner. DMA measures stiffness and damping, which are reported as modulus E and tan δ [38]. For viscoelastic materials such as rubber, the modulus consists of the storage modulus and the loss modulus (see Section 2.2). The ratio of the loss to the storage modulus is then the tan δ, which is a measure of damping.

DMA operation is illustrated in Fig. 4.2. In DMA, when a sample is subjected to a sinusoidal oscillating stress as in picture 1a of the figure, it will respond with a similar strain wave. With a perfectly elastic response, an in-phase storage response is seen as in 1b. When the response is viscous, an out-of-phase loss response is seen as in 1c. Real viscoelastic materials as in 1d, will fall within these two extremes, and the phase angle δ and amplitude at peak k, shown in the figure, can be used for calculation of the viscoelastic modulus E and damping as tan δ.

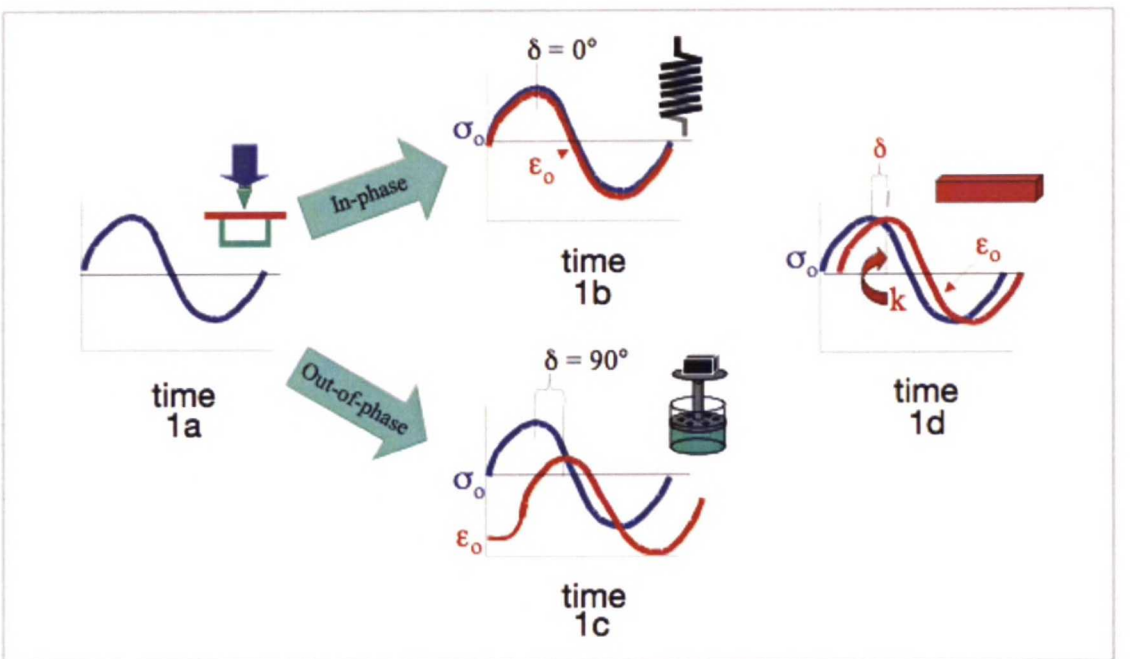

Figure 4.2: Illustration of DMA operation. Picture 1a shows a sinusoidal stress acting on the sample, 1b shows an in-phase strain response of an elastic material and 1c an out-of-phase strain response of a viscous material. Picture 1d depicts the strain response of a real viscoelastic material with the phase angle δ and amplitude at peak k. [39]

4.3 Durometry

Durometry is a hardness measurement for materials such as rubber and plastic using an indentor. The deformation caused by indentation into a solid is governed by linear elastic mechanics [40]. The penetration depth in an elastomer may change over time so it is important to be consistent in recording the reading of a durometer.

Shore hardness is a measure of the resistance of a material to penetration of a spring loaded needle-like indentor. Shore A scale is used for testing soft elastomers

and other soft polymers. The letter A in the Shore scale refers to the geometry and loading force of the needle in the durometer. The scale ranges from 0 to 100. The value 0 corresponds to maximum penetration of the durometer needle, while 100 stands for zero penetration.

4.4 Rubber samples

For the experimental part, tyre rubber samples were received from Nokian Tyres. Each sample was a rubber block of 1 cm thickness and laterally a square of 6 cm side length. The manufacturer also provided us with DMA data about the rubber compound of the samples. The glass transition temperature of the rubber compound is -16°C, taken as the temperature at maximum loss tangent.

The samples are labeled S1–S5. The rubber blocks were glued on an aluminum sample holder, which could be attached firmly to the slider of the linear friction tester. A photograph of sample S5 after run-in, which was carried out for each sample, is presented in Fig. 4.3. For the linear friction testing, an arrow was drawn on each sample holder to retain the same sliding direction throughout the experiments.

Figure 4.3: Photograph of tyre rubber sample S5 after run-in.

4.5 Linear friction testing

Experiments were conducted with a linear friction tester in a climate chamber to measure the sliding friction for the five samples described in the previous section.

The substrate was a worn real road asphalt surface. A side view of the apparatus is shown in Fig. 4.4.

The temperature in the climate chamber was controlled between -8°C and +32°C for the experiments. The largest temperature changes were carried out over night to allow for the brick walls of the climate chamber, the asphalt and other objects of considerable heat content to reach the target temperature before the friction measurements. Thus a stable ambient temperature was maintained during the measurements of friction at various sliding speeds. A temperature sensor located at the same height as the asphalt surface was used to assess the temperature in the climate chamber.

Humidity in the atmosphere is a very important consideration for any measurement of friction. However, direct control of humidity in the climate chamber was not possible and only temperature was thus controlled. Allowing enough time before measuring after changing the temperature also helps to prevent excess condensed water being on the substrate or sample surfaces.

The sliding speed could be controlled between 10^{-3} m/s and 10^{0} m/s with such high precision that the uncertainty in the sliding speed is not considered in our results as it is relatively very small compared to other sources of uncertainty in the measurement. This precision is realized with a servo motor, which is used to control the sliding. The applied vertical load was set to 500 N. Hence, the nominal contact pressure was approximately 0.14 MPa. The variation in the vertical load is assessed in the results in Section 5.1.

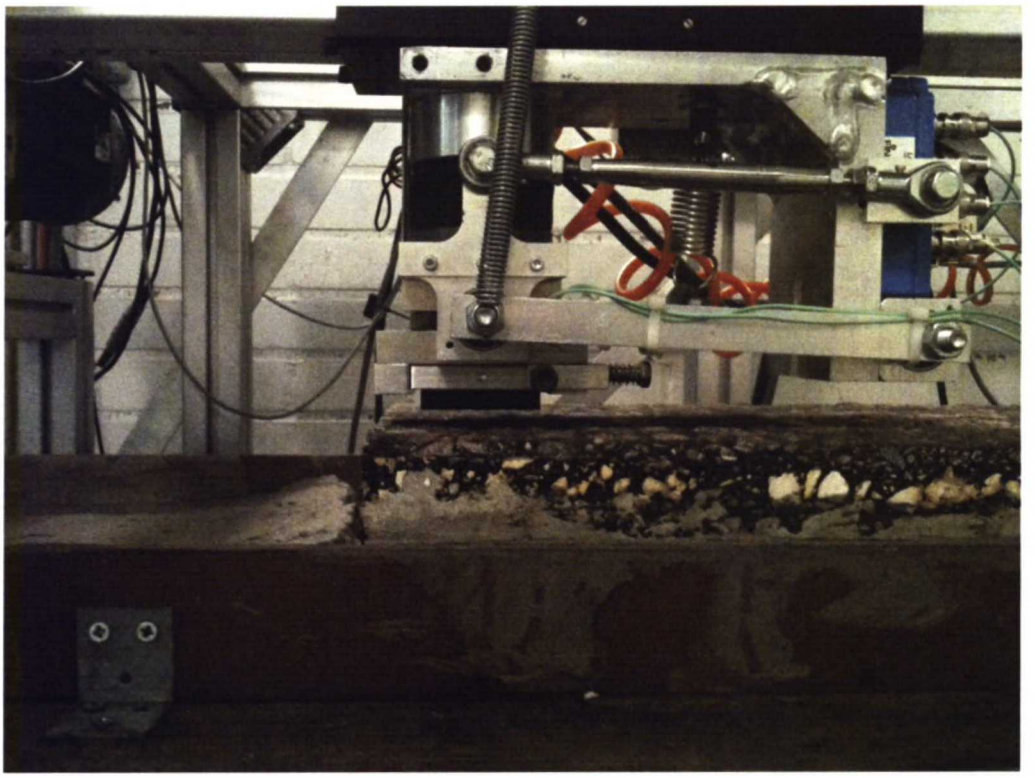

Figure 4.4: Photograph of the linear friction tester showing the slider at the initial position with an attached sample.

Longitudinal and vertical forces were measured during the sliding of the rubber block on the asphalt substrate every 0.2 mm in the sliding distance. The total sliding distance was 30 cm and the acceleration requested from the apparatus to reach the target sliding speed was 8 m/s^2. A view of the measurement setup from the end of the asphalt is presented in Fig. 4.5.

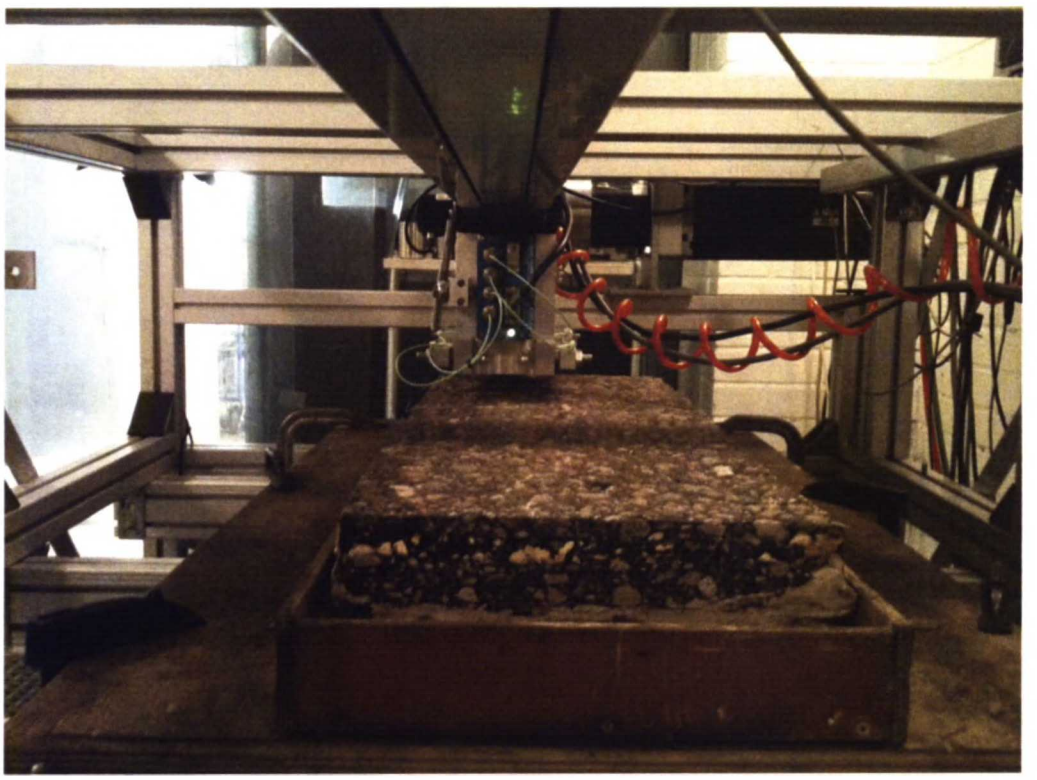

Figure 4.5: Photograph of the linear friction tester showing the asphalt and the slider at the initial position. The friction test was carried out over 30 cm from the initial position towards the camera.

Due to the mechanics of the device, the requested acceleration may not be reached exactly, especially at the very beginning. Hence, assuming an acceleration of 7 m/s^2, the final constant speed for the measurement was acquired over a distance of about 7 cm for the target speed of 1 m/s. For the lower speeds, this distance is even shorter. The deceleration at the end of the sliding distance was assumed to be similar to the acceleration at the beginning. From the gathered data, the local friction coefficients can be obtained over the whole sliding distance and to calculate one value for each speed, the mean value over the distance of 13–23 cm from the initial position is used. This is done to exclude the effects of the acceleration and deceleration of the slider at the beginning and end, respectively.

Furthermore, the longitudinal and vertical forces F_x and F_z are mechanically coupled and not indepedent. Observing the shaft in Fig. 4.4, we note that when the sample is pressed against the asphalt under load, the left end of the shaft will be lower than the right end. Pulling from the right end of the shaft will thus result in a force along the shaft with an upward component. This means that the friction force F_x that has to be overcome by the apparatus has a tendency to decrease the vertical force F_z. This interaction and its effect on the value of the friction coefficient is considered in the results in Section 5.1.1.

The same set of measurements was conducted two times in order to assess the repeatability of the results and wear of the rubber, so the temperature was varied

between -8°C and +32°C two times during the measurements. Such a set of measurements of the friction coefficient as a function of sliding speed at our predefined temperatures will be refer to as a *temperature cycle*. The ambient temperature was let to stabilize at about -8°C, +5°C, +21°C and +32°C in one temperature cycle. In addition, in the first temperature cycle, the friction coefficient was measured against the sliding speed at +1°C.

In accordance with the phenomenological Mullins' effect (see Section 2.2.6), a run-in was conducted for all samples. This was done by applying a vertical load of 700 N on the rubber samples in the linear friction tester and sliding them against the asphalt surface with a very low speed of 2 mm/s for a distance of 20 cm. The load was intentionally set higher for the run-in than for the actual friction tests, in which 500 N was used, to gain repeatability in the stress-strain behaviour of rubber according to the Mullins' effect. The observed run-in effect is discussed in Section 5.1.2.

In order to keep the measurement conditions constant, we cleaned both the sample surface and the asphalt surface in the sliding area with pressurized air after every second measurement in the first temperature cycle. By a measurement we mean sliding the rubber one time over the distance of 30 cm, as explained earlier. In the second temperature cycle the cleaning was done only after every third measurement, in order to speed up the measurement.

In the linear friction testing, our purpose is to measure the friction coefficient against sliding speed at various temperatures. This is done to assess both the effect of the ambient temperature and the effect of the *flash temperature* on the frictional properties of rubber. Finally, the aim is to validate the Persson hot friction model through comparison with our experimental results.

5 Results and discussion

The sliding friction coefficient was measured as a function of sliding speed and temperature for tyre rubber samples on asphalt in a climate chamber, as explained in Section 4.5. The experimental results are presented and discussed in this section. Firstly, an interpretation of the results in the distance domain and substantiation of the method, in which the experimental data are processed, are presented. The run-in and wear of the samples are then discussed. This is followed by an analysis of the results for sliding friction coefficient as a function of the sliding speed and temperature. Ultimately, the experimental results are juxtaposed with the Persson hot friction theory predictions and the similarities and differences analyzed.

5.1 Friction as a function of sliding distance

The results for the local friction coefficients measured over the whole sliding distance of 30 cm for a set of speeds in the range 10^{-3} m/s – 10^{0} m/s during the first temperature cycle at -8°C are presented in Fig. 5.1. The nature of the friction exhibited by the slider-substrate system in the linear friction tester substantiates the data processing we applied to yield the coefficient of sliding friction for each sliding speed.

In Fig. 5.1 one can see that the sequence of the friction coefficients with respect to the sliding speed remains over the whole sliding distance of 30 cm, except for the very beginning, so averaging over sliding distance to yield the friction coefficient for each sliding speed produces consistent results. At the beginning, roughly over the first centimeter, we measure friction before sliding, seen as the highest peak reaching over 1.2, and after the peak we observe the transition to sliding friction. Hence, a consistent value for the sliding friction coefficient can indeed be obtained by calculating the mean value over the distance of 13 cm – 23 cm from the initial position of the slider, as explained in Section 4.5. In this way we avoid the effects of acceleration and deceleration at the beginning and end, seen as increasing and decreasing friction, respectively.

It is interesting to note that the sliding friction coefficient first increases going from a sliding speed of 1 mm/s to 5 mm/s and then decreases systematically for higher sliding speeds. An analogous trend is observable at each measured temperature in both temperature cycles. We assess the sliding speed dependency of the sliding friction coefficient in more detail below.

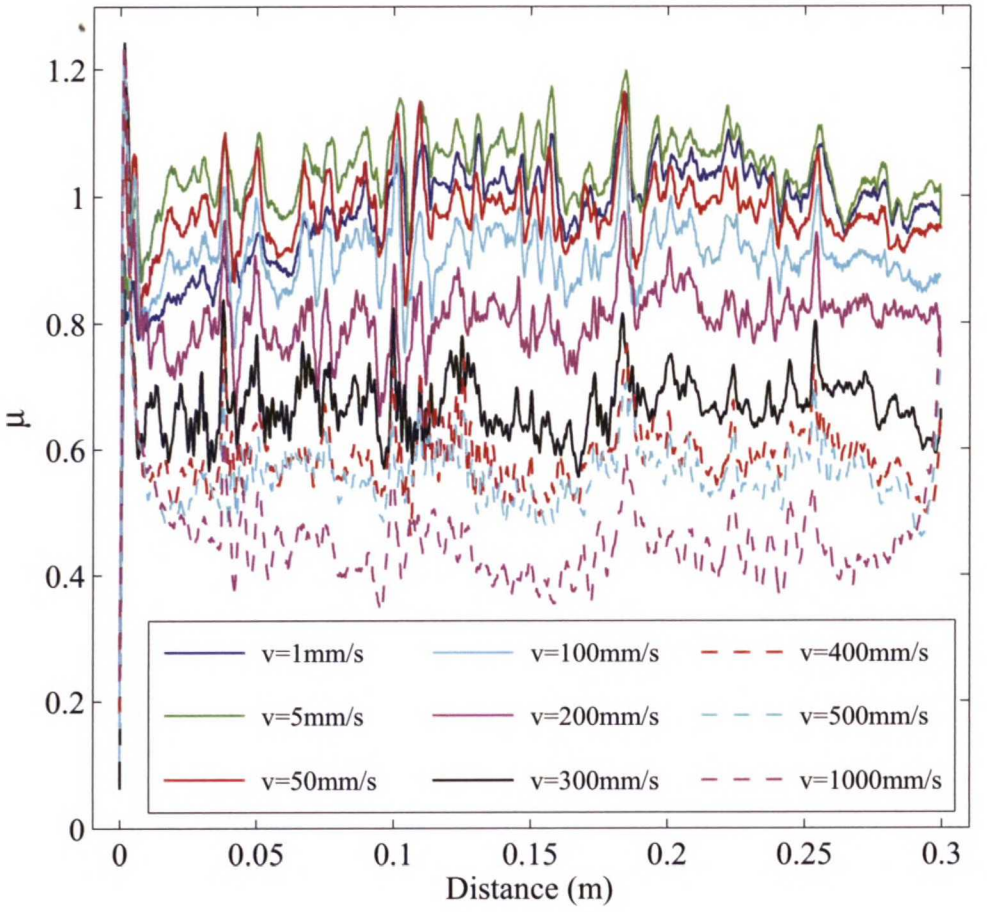

Figure 5.1: Friction coefficient versus sliding distance at -8°C for sliding speeds 1 mm/s – 1000 mm/s during the first temperature cycle.

Furthermore, one notes in Fig. 5.1 that the friction peaks are of an approximate width of 1 cm. This width matches the size of the greatest surface roughness of the asphalt substrate, namely the largest stones in the asphalt. By this observation then, it is worth further noting, that although the side length of the rubber sample is 6 cm, the biggest surface roughness is reproduced in the friction peaks. Hence, the highest friction could arise in the leading edge of the rubber slider, possibly in the Schallamach wave mechanism [41]. In Fig. 4.4 and 4.5, one can observe these largest-sized, paler colored stones sticking out from the otherwise darker grey asphalt surface. On the other hand, the explanation for the peaks may be simply the mechanical discontinuity of the finite-sized rubber block and the introduction of the roughness from the stones at the leading edge.

5.1.1 Vertical load and frictional force

By the definition $\mu = F_x/F_z$, the variation in the friction coefficient μ can originate from either a variation in the vertical load F_z or a variation in the actual longitudinal friction force F_x. Thus the results were analyzed to see how the two forces are changing during a measurement, and if the nominal pressure is actually constant.

It was found that the apparatus can maintain a rather constant vertical load throughout a measurement, which is illustrated for a measurement at +21°C in Fig. 5.2a. This measurement involves highest variation in the forces from all the measurements. We note in the figure that the variation from the 500 N target of the vertical load is less than 50 N over the whole sliding distance, even at the highest resonance amplitude of the friction force. The behaviour of the vertical load with respect to the friction force is similar for all measurements. We thus conclude that the variation of the vertical load is within ±10 % for our results and so we have a rather constant nominal pressure. Averaging over the sliding distance also diminishes any effects from an oscillating nominal pressure. The resonance vibration observed for the frictional force and consequently for the friction coefficient in the figure is analyzed in more detail in Appendix D. We simply note here that the resonance vibration arises in the whole apparatus during the measurement and is not inherent to the rubber material itself.

By assessing the sensitivity of the friction coefficient μ to changes in the vertical load F_z and the friction force F_x with differentials, we note that the sensitivity depends on the proportion of the magnitudes of F_x and F_z

$$\Delta\mu = \left|\frac{1}{F_z}\Delta F_x\right| + \left|\frac{F_x}{F_z^2}\Delta F_z\right| \tag{60}$$

Setting $F_x = F_z$, as is approximately the case in our measurements, as the friction coefficient is close to one, when averaging F_x over the distance, we obtain the same sensitivity for μ to a change ΔF_x and ΔF_z

$$\Delta\mu = \frac{1}{F_z}\Delta F_x + \frac{1}{F_z}\Delta F_z \tag{61}$$

Thereby, a considerable change in the friction coefficient in our results can be attributed to a corresponding change in the actual friction force, as we know that the maximum change in the load is within ±10 %. This is corroborated by Fig. 5.2b, which shows the friction coefficient on the left y-axis and the friction force on the right y-axis as a function of sliding distance for v = 1000 mm/s at +21°C. One observes that the friction coefficient and friction force curves feature a very similar pattern.

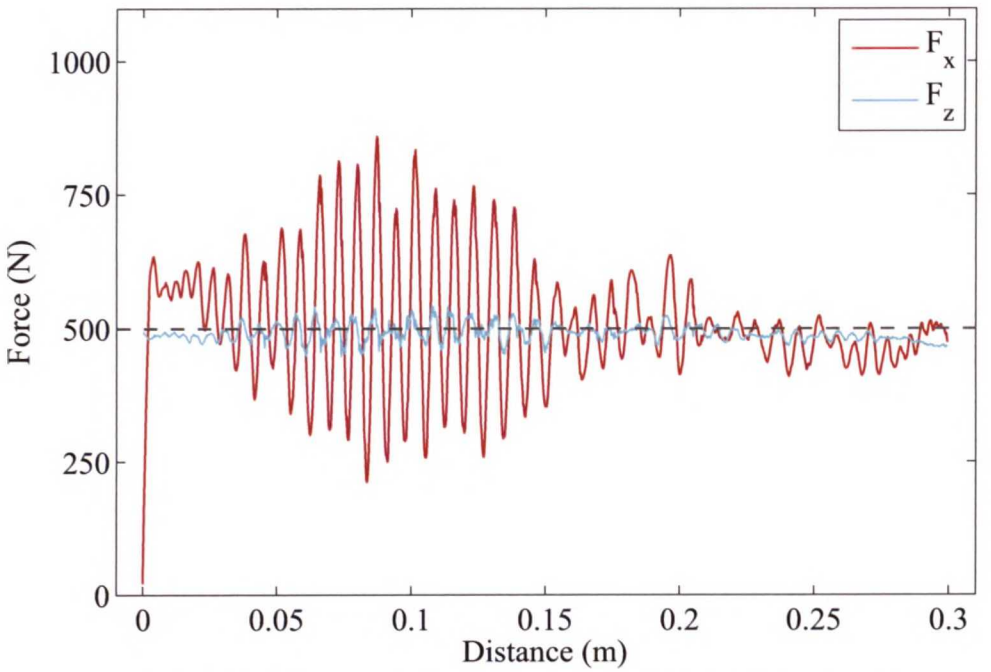

(a) Friction force and normal force as a function of sliding distance.

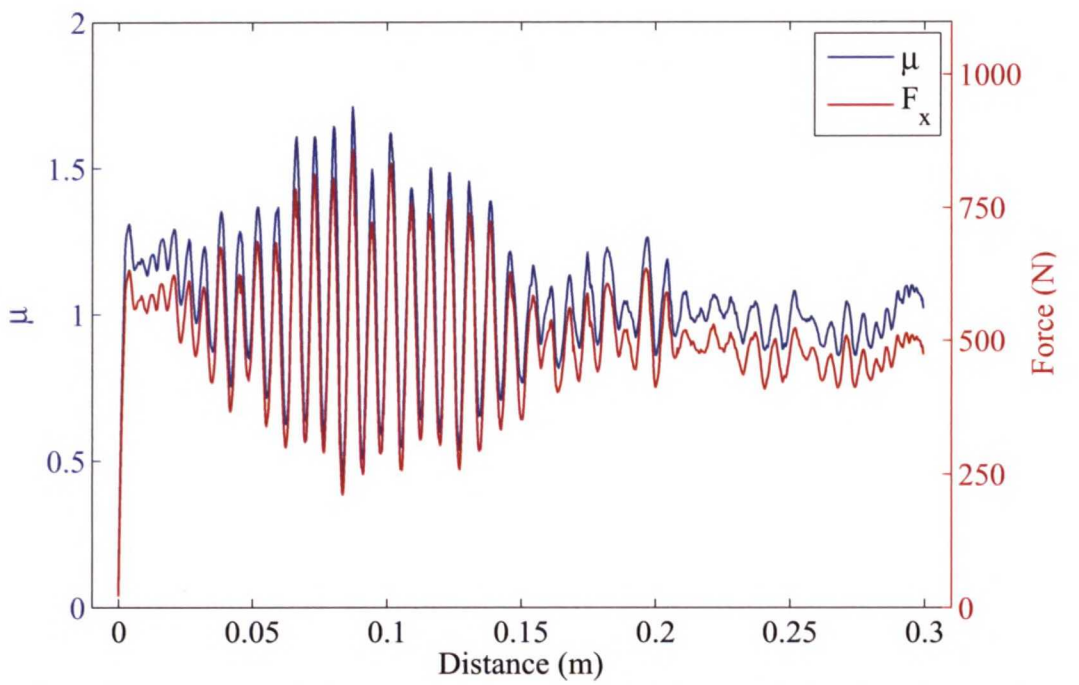

(b) Friction coefficient (left y-axis) and friction force (right y-axis) as a function of sliding distance.

Figure 5.2: Illustration of variation in the friction force and normal force and the effect on the friction coefficient in a linear friction test with v=1000 mm/s at +21°C.

It is further noted that the above sensitivity analysis and the conclusion about the dominance of the actual friction force in the behaviour of the friction coefficient apply for both the local, roughness induced friction peaks, which were observed to roughly reproduce the roughness size of the stones, and the resonant vibration. The conclusion was demonstrated above for one friction measurement and we checked this in all other results as well.

5.1.2 Run-in and sample wear

Before the actual friction measurements, the run-in was carried out for the new rubber samples. The Shore A values of the samples S1–S5 before and after run-in are presented in Table 5.1. It is noted that the Shore A values of the samples measured before the run-in overlap, when taking into account the uncertainty of ± 2 in the values. Thus we conclude that the hardness characterized by Shore A (see Section 4.3) is essentially the same for all samples and thus the choice of sample in the measurement should not affect the results.

The shore A after run-in looks similar for all samples, too, when taking into account the uncertainty in the durometry. Overall, the mean Shore A of the samples drops by 4.8 from a mean value of 77.0 down to 72.2 for all samples during the run-in. This indicates that the rubber becomes softer, which is in accordance with the Mullins' effect.

The Shore A was measured after all the friction measurements as well, and as can be seen in Table 5.1, the hardness values did not change after the run-in to a considerable extent, but rose by 1. This rise, indicative of a slight hardening of the rubber material, may be due to the time of the measurement - the values for Shore A after run-in were measured within hours after ending the measurement, whereas the values after all the measurements were recorded weeks afterwards. Sample S5 is the reference, which was not used in the actual friction measurements. It is noted that the Shore A value of S5 is similar within the uncertainty to the Shore A of the other samples after the friction measurements were conducted on them. Thus the conclusion is that the softening or hardening of the rubber material is not a cause of remarkable changes in the friction after the run-in process during the actual friction measurements.

Table 5.1: The run-in effect of rubber. Shore A values measured with a durometer for the samples before and after run-in at +21°C. The last column shows the mean value of all samples and the standard deviation (stdev).

Sample	S1	S2	S3	S4	S5	Mean ± stdev
Shore A before run-in (±2)	76	77	78	77	77	77.0 ± 0.7
Shore A after run-in (±2)	73	70	72	73	73	72.2 ± 1.3
Shore A after all measurements (±2)	73	73	73	73	74	73.2 ± 0.4

The run-in method was thereby successful and enhances the repeatability in the

friction tests as anticipated. Next, we will assess the effect on friction of the softening of the rubber during the run-in process, and in particular, the change in the friction coefficients of the samples during the measurements.

As seen in Table 5.2, there is rather large variation of over 10 % between the samples in the initial friction that they exhibit on the asphalt, as opposed to the Shore A values, which were essentially the same for all samples in the durometry. One crucial difference between the sliding friction coefficient and the Shore A measurement is that the sliding friction coefficient is measured over a distance. As the rubber undergoes the run-in process during the first slide, the rubber properties will consequently change during sliding. This may explain the large variation in the first measurement friction values.

Table 5.2: Friction coefficients in the first test before run-in with F_z = 400 N and v = 1 mm/s at +21°C.

Sample	S1	S2	S3	S4	S5
μ in the first measurement	0.99	0.86	0.93	0.87	0.89

The sliding friction coefficient for samples S1–S4 after the first temperature cycle and for reference sample S5 after the run-in are presented for three different sliding speeds at +21°C in Table 5.3. As compared to samples S1–S3, which were used at one temperature each, S4 was used at two different ambient temperatures, so it has been slid two times as much. There is considerable variation in μ between the samples, which may be partly due to difference in wear during the friction measurements at different temperatures but also due to other experimental uncertainty. Wear of the samples is described in Appendix E. The uncertainty in the measurement for μ by the standard deviation is 10 % or greater for all values. Considering the uncertainty then, the friction values in the table are roughly the same, and we cannot draw a conclusion whether there is a difference in wear at different temperatures.

Table 5.3: Sliding friction coefficient for all samples measured at +21°C after all measurements in the first temperature cycle. The original measurement temperature for each sample is shown on the row under the sample labels. Sample S5 was not used in the measurements and is thus a reference after run-in.

Sample	S1	S2	S3	S4	S5
Original measurement T (°C)	+21	+32	+5	-8, +1	-
μ with v = 1 mm/s	1.13	1.16	1.07	1.28	1.12
μ with v = 100 mm/s	1.15	1.19	1.23	1.35	1.28
μ with v = 1000 mm/s	1.12	1.13	1.16	1.14	1.14

5.2 Friction as a function of sliding speed and temperature

The sliding friction coefficient μ as a function of sliding speed v and ambient temperature for the first and the second temperature cycle is presented in Fig. 5.3a and Fig. 5.3b, respectively. The uncertainty in μ shown in the error bars is calculated as the standard deviation over the sliding distance. The uncertainty of the ambient temperature is about ± 1°C, corresponding to the maximum variation in the reading of the temperature sensor during the measurements.

There is a systematic trend in the behaviour of the friction coefficient as a function of sliding speed for all measured temperatures. Thus, smoothing by spline functions was applied to the results to interpolate between the measurements and find the maximum friction point along the fitted curve, as no underlying function is known *a priori* [42]. MATLAB curve fitting tool with a spline smoothing parameter of 0.98 was used to compute the fit.

As seen in the computed spline fits shown in Fig. 5.3, at first the sliding friction coefficient μ slightly increases with increasing sliding speed, from a value above one at $v = 1$ mm/s by a maximum of 0.1 at all temperatures. The sliding speed at which the rubber-asphalt system exhibits maximum sliding friction clearly depends on the ambient temperature. After the peak value, we observe the friction coefficient decreasing with increasing sliding speed down to less than one at $v = 1$ m/s at temperatures +5°C, +1°C and -8°C in the first temperature cycle and at temperatures +5°C and -8°C in the second temperature cycle. For the other temperatures, the lowest friction coefficient observed is approximately one.

We note that the results exhibit a high degree of similarity between the first and the second temperature cycle, regardless of the rather high nominal contact pressure of 0.14 MPa and the resulting wear of the samples, and other possible changes in experimental conditions. The absolute difference in μ between the cycles measured for the same sliding speed and temperature is roughly within 0.1 for all the other temperatures except for -8°C, at which there is a difference of about 0.2 at $v = 1$ m/s.

Most importantly, we note that the trends look rather similar: maximum friction μ_{max} is measured at approximately the same speed for T = -8°C and T = +21°C, as seen in the results of the interpolation using spline fitting presented in Table 5.4 and Table 5.5. Also for T = +5°C, the sliding speed at the friction peak is of the same order of magnitude, whereas for T = +32/31°C (1°C difference between first and second cycles) this seems not to be the case. However, if one considers the uncertainty in μ at T = +32/31°C in Fig. 5.3, one observes that, within the uncertainty, maximum friction could be found at the same order of magnitude in sliding speed in both temperature cycles. Overall, all the μ_{max} values are slightly greater for the second temperature cycle than for the first, so there could be some run-in effect in terms of the friction during the first temperature cycle, although this was not observed in the hardness measured by the Shore A values (see Section 5.1.2).

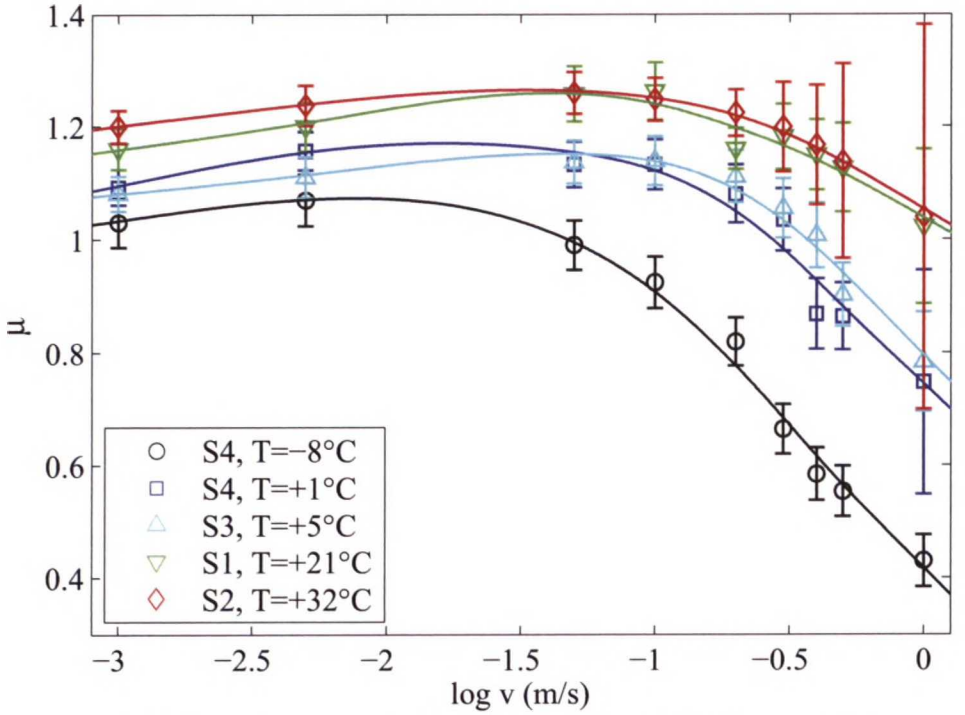

(a) First temperature cycle. We measured additionally at +1°C.

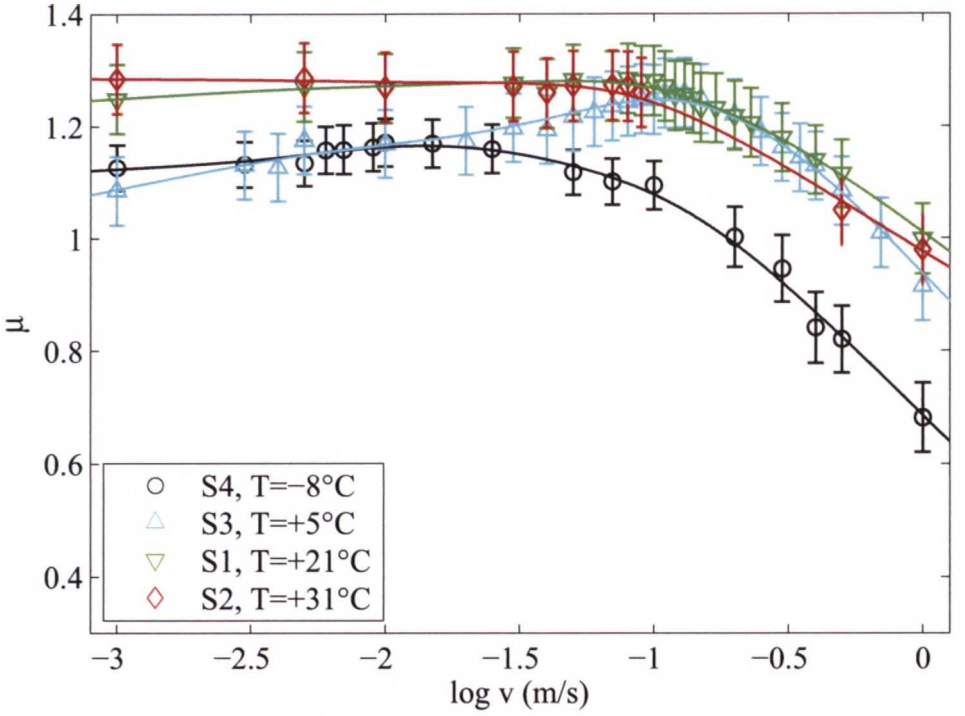

(b) Second temperature cycle. Note the difference of 1°C in the highest temperature measured to the first cycle.

Figure 5.3: Friction coefficient versus sliding speed for ambient temperatures T_0 = -8°C – +32°C.

Table 5.4: Maximum friction and the corresponding sliding speed in the interpolation by spline fit to the results in Fig. 5.3a using the least-squares method with R-squared goodness of fit values shown.

Ambient temperature	-8°C	+1°C	+5°C	+21°C	+32°C
μ_{max}	1.07	1.17	1.15	1.26	1.26
v @ μ_{max} (mm/s)	7.4	16.8	44.2	41.0	32.8
R-squared	0.99	0.95	0.97	0.94	0.99

Table 5.5: Maximum friction and the corresponding sliding speed in the interpolation by spline fit to the results in Fig. 5.3b using the least-squares method with R-squared goodness of fit values shown.

Ambient temperature	-8°C	+5°C	+21°C	+31°
μ_{max}	1.17	1.24	1.28	1.28
v @ μ_{max} (mm/s)	14.2	100.0	49.8	1.0
R-squared	0.99	0.98	0.99	0.99

Finally, one notes that most of the error bars in Fig. 5.3a and Fig. 5.3b overlap for similar temperatures and sliding speeds. Hence, we conclude that the results are consistent enough about the trend in the sliding speed dependency of the sliding friction coefficient for comparison with theoretical model predictions but the absolute friction level has an uncertainty of about 10 % or greater.

In the first temperature cycle, an additional measurement at T = +1°C was conducted to assess the effect of changing the temperature in the climate chamber. The conclusion is that no systematic error seems to arise from whether we are going up or down in the ambient temperature of the climate chamber and also the T = +1°C results agree well with the overall trend in the friction level and the sliding speed for maximum friction.

There are data points missing in the 10^{-1} – $10^{-0.5}$ m/s sliding speed range. The reason for this is that the sample S2 was damaged during the measurement a rubber piece came off the surface at the leading edge, so the corresponding data points were removed as outliers but the last two seem to fit the trends well. This also shows that the measurement conditions are rather rough for the samples and the repeatability is thus by no means self evident *a priori*.

Not only did the rubber residue cause a problem in the S2 measurement but also rubber dust was constantly coming off the sample surface and ending up on the asphalt due to wear. This is why both surfaces were cleaned using pressurized air at constant intervals. However, the cleaning was done less frequently during the second temperature cycle (after every third measurement) than in the first temperature cycle (after every second measurement). This could affect the results, but one

cannot observe a pattern before and after cleaning the surfaces, so the effect of rubber residue is unlikely to be remarkable.

5.2.1 Velocity dependency of sliding friction

Figure 5.4 shows the loss tangent $\tan\delta = \operatorname{Im} E / \operatorname{Re} E$ as a function of temperature T and frequency ω. DMA data was used for the viscoelastic modulus E and the WLF equation was used to shift the frequency as a function of temperature. The figure can be used to explain some of the behaviour of sliding friction as a function of temperature and sliding speed that was measured. As seen in the figure, the peak of the loss modulus shifts to higher frequencies with an increasing temperature.

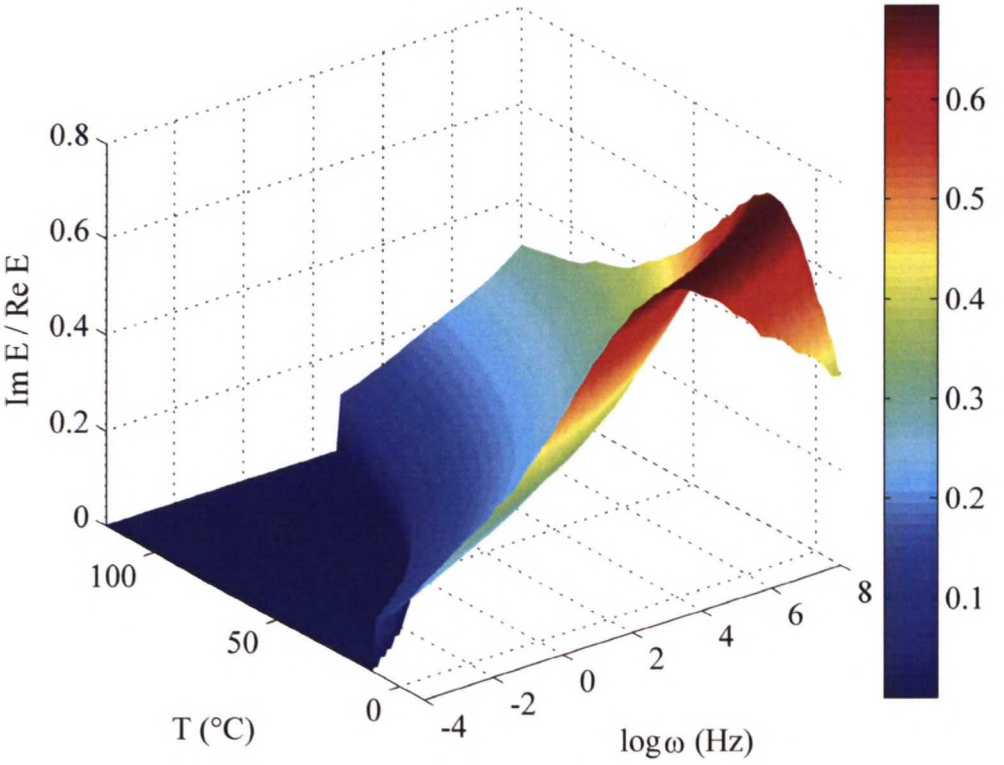

Figure 5.4: Loss tangent of rubber $\tan\delta = \operatorname{Im} E / \operatorname{Re} E$ (colorbar shown on the right) as a function of temperature T and frequency ω. DMA data and the WLF equation were used to calculate the loss tangent.

The same plot in 2D is presented in Fig. 5.5. The trajectories labelled a–e in the figure elucidate some of the behaviour of sliding friction as a function of temperature and sliding speed that was measured and is presented in Fig. 5.3, as the internal friction of rubber is governed by the loss tangent $\tan\delta$ [5]. By recalling that the perturbing frequency of the rubber from a rough surface with roughness wavevector q is directly proportional to the sliding speed v as $\omega \sim q\,v$, given constant roughness, we can relate the frequency axis to the sliding speed in Fig. 5.5. To calculate

the trajectory for each sliding speed, we used the range of roughness wavevectors $q_0 = 800$ to $q_0 * \xi_{max} = 320000$, corresponding to roughness size range 10^{-5} m to 10^{-2} m. $q_0 = 800$ was measured (see Appendix F) and $\xi_{max} = 400$ is from [5]. The Persson hot friction theory implemented in this work was used to compute the temperatures corresponding to each frequency of perturbation.

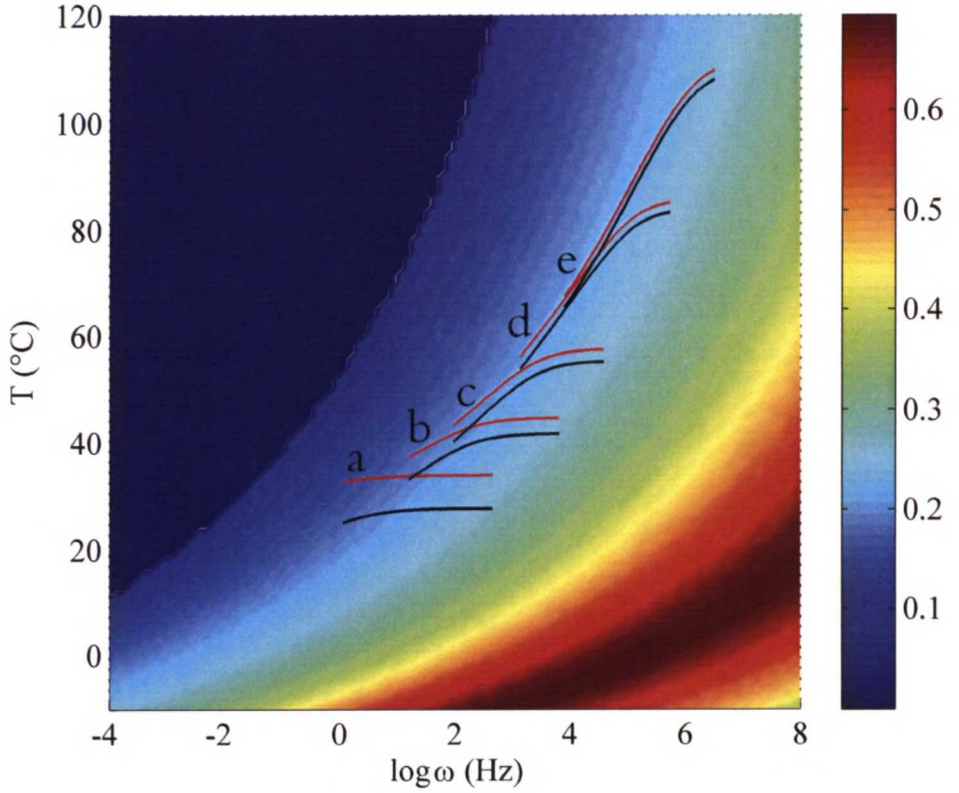

Figure 5.5: Loss tangent of rubber (colorbar shown on the right) as a function of temperature T and frequency ω. DMA data and the WLF equation were used to calculate tan δ. The black ($T_0 = +21°C$) and red ($T_0 = +32°C$) trajectories illustrate the operating frequency and temperature range of the rubber for constant sliding velocities marked with letters a–e, which correspond to a: v $\approx 10^{-3}$ m/s, b: v $\approx 10^{-2}$ m/s, c: v $\approx 10^{-1}$ m/s, d: v $\approx 10^{0}$ m/s, e: v $\approx 10^{1}$ m/s.

Observing the trajectories in Fig. 5.5, we note that going from v $\approx 10^{-3}$ m/s denoted by 'a' to v $\approx 10^{-1}$ m/s denoted by 'c', for instance, the trajectory is overall on a higher loss tangent for the higher sliding speed, which explains the increasing sliding friction with increasing sliding speed in this sliding speed range in Fig. 5.3a for both $T_0 = +21°C$ (black trajectories) and $T_0 = +32°C$ (red trajectories). Observing Fig. 5.5, it also easy to understand why the flash temperature effect decreases the sliding friction as compared to cold friction without considering the frictional heating: if we used the ambient temperature for all perturbation frequencies, the trajectories would be straight horizontal lines in the figure, and clearly reach to a

higher loss tangent, especially with the higher sliding speeds.

In Fig. 5.5, we further note that the loss tangent is slightly lower for $T_0 = +32°C$ (red trajectories) than for $T_0 = +21°C$ (black trajectories) for the same sliding speeds, which would also suggest lower sliding friction, but this is not the case according to the experimental results in Fig. 5.3. Thus the conclusion is that the loss tangent gives good qualitative indication about sliding friction as a function of sliding speed at least up to speeds on the order of 1 m/s (highest speed measured to compare), when the flash temperature effect is taken into account. However, to better explain the behaviour of the overall friction level as a function of ambient temperature and sliding speed, a more advanced model is needed.

5.3 Persson model validation through comparison with experiments

Sliding friction coefficients were computed as a function of sliding speed using the implementation of the Persson hot friction theory written for this work. The experimental and theoretical parameters used in the model are listed in Table 5.6. The Hurst exponent H and the roll-off wavevector q_0 were obtained using profilometry (see Appendix F). For the viscoelastic behaviour of the rubber we use DMA data from the manufacturer. Where the perturbation frequency is outside the measured range, we use the SLS model to approximate the modulus. The transition to the SLS model from the DMA data is seen in Fig. 5.4. But as seen in Fig. 5.5, the perturbation frequencies are mostly inside the range of the DMA data.

Table 5.6: List of experimental and theoretical parameters used in the Persson friction model calculation.

Parameter name	Parameter	Value	Origin
Hurst exponent	H	0.84	Profilometry
Roll-off wavevector	q_0	800	Profilometry
Nominal pressure	σ_0	0.14 MPa	Friction test
Ambient temperature	T_0	+21°C, +32°C	Friction test
Glass transition temperature	T_g	-16°C	DMA
Macro-asperity zooming factor	ξ_m	3.5	Theoretical [5]
Poisson ratio	ν	0.5	Empirical [5]
Mass density	ρ	1000 kg/m^3	Empirical [5]
Heat capacity	C_V	1000 J/K	Empirical [5]
Rms roughness amplitude	h_0	$1.25 \cdot 10^{-3}$ m	Theoretical [5]

The spline fit to the experimental results of Fig. 5.3a at +21°C and the corresponding Persson model prediction are presented in Fig. 5.6. The Persson model was scaled with a free parameter (0.1315) to match the level of maximum friction measured, so we can only compare the trend as the maximum friction level predicted

by the model is approximately eightfold as compared to the experiment. It is noted that the model prediction is qualitatively similar to the experiment, except that the sliding speed corresponding to maximum friction is too low by approximately two orders of magnitude.

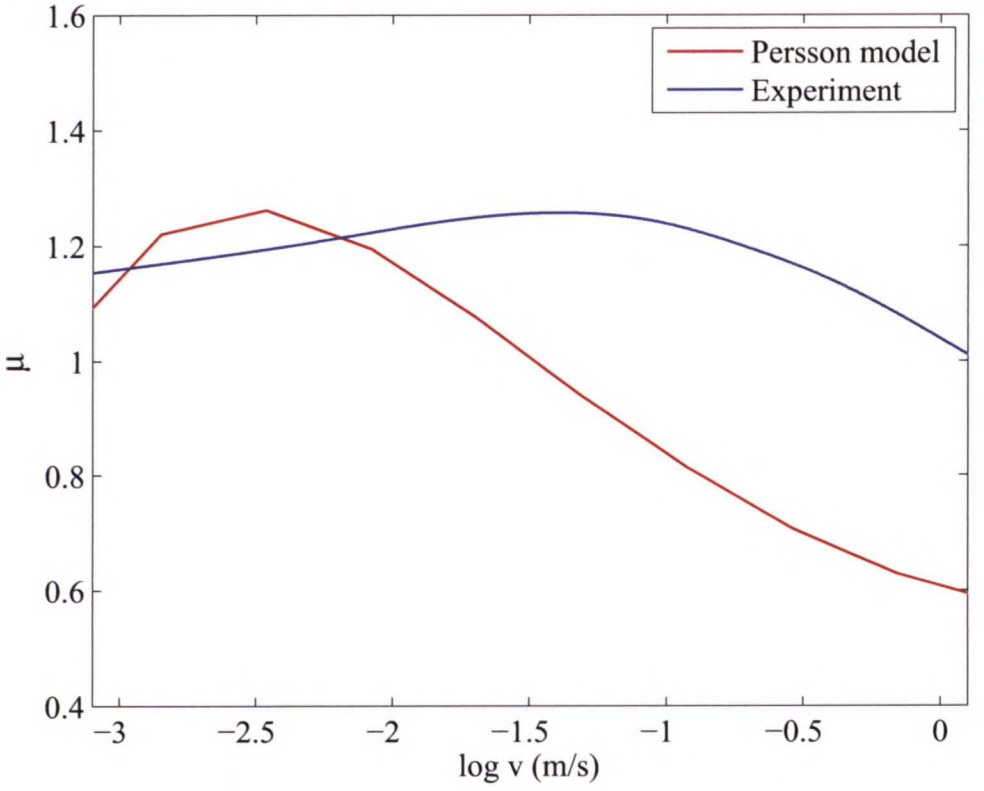

Figure 5.6: Comparison of Persson rubber friction model with experiments at +21°C. Free parameter used in scaling Persson model = 0.1315.

Similar comparison between the Persson model and experiment at +32°C is presented in Fig. 5.7. The experimental result is the spline fit of Fig. 5.3a at +32°C. Also here the Persson model was scaled with a free parameter (0.2541) to match the magnitude of maximum friction in the experiment. So also for this temperature, the model prediction for the maximum friction is clearly greater than that measured in the experiment, approximately fourfold. However, the sliding speed at maximum friction predicted by the model matches now well that measured in the experiment.

At both temperatures, the model prediction of the sliding friction is too sharp with respect to the sliding speed. In other words, without scaling the maximum friction predicted by the model is many times that measured in the experiment, and with scaling the lowest friction level predicted by the model is a fraction of that measured in the experiment. Decreasing sliding friction with increasing sliding speed from the peak friction can be explained by increasing perturbation frequency and correspondingly increasing temperature and lowering loss tangent (see Section 5.2.1).

Hence, after scaling to match the maximum friction level, the model predicts the sliding friction beyond the maximum friction point well for +32°C as seen in Fig. 5.7 and the same would apply for +21°C in Fig. 5.6, if the curve was translated to higher sliding speeds to match the sliding speed for maximum friction.

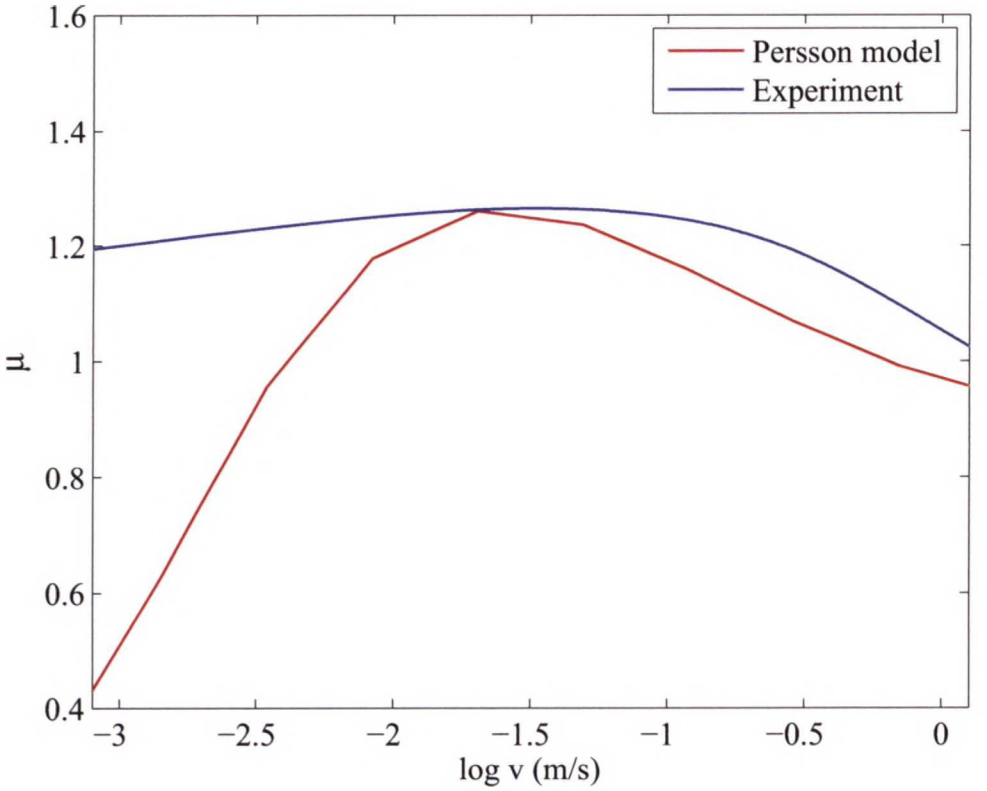

Figure 5.7: Comparison of Persson rubber friction model with experiment at +32°C. Free parameter used in scaling Persson model = 0.2541.

To explain too low sliding friction predicted by the model at lower sliding speeds than that for maximum friction, seen clearly in Fig. 5.7 and as a similar trend to part in Fig. 5.6, we recall that the Persson hot friction theory only takes into account the energy dissipation in the rubber bulk due to deformations. Hence, the difference between the Persson model and the experiment at such low sliding speeds can be attributed to energy dissipation by shearing a thin, confined contamination film and energy dissipation by crack opening at the interface [13], which are not taken into account in the Persson model. The importance of such energy dissipation mechanisms increases with lower sliding speeds and corresponding lower perturbation frequencies of the rubber, as the storage modulus of the rubber decreases and the area of real contact increases.

The flash temperature as a function of sliding speed predicted by the model for ambient temperatures T_0 of +21°C and +32°C is presented in Fig. 5.8. As seen in the figure, the behaviour of the flash temperature is very similar at both ambient

temperatures, with the exception that the flash temperature rises more rapidly at T_0 =+21°C for low sliding speeds of v = 10^{-4} m/s – 10^{-2} m/s. Going to higher sliding speeds, the flash temperatures at the two different ambient temperatures come very close to each other, with a difference on the order of 1°C beyond v = 10^{-1} m/s. This explains the similar sliding speed behaviour of the sliding friction at the two different ambient temperatures.

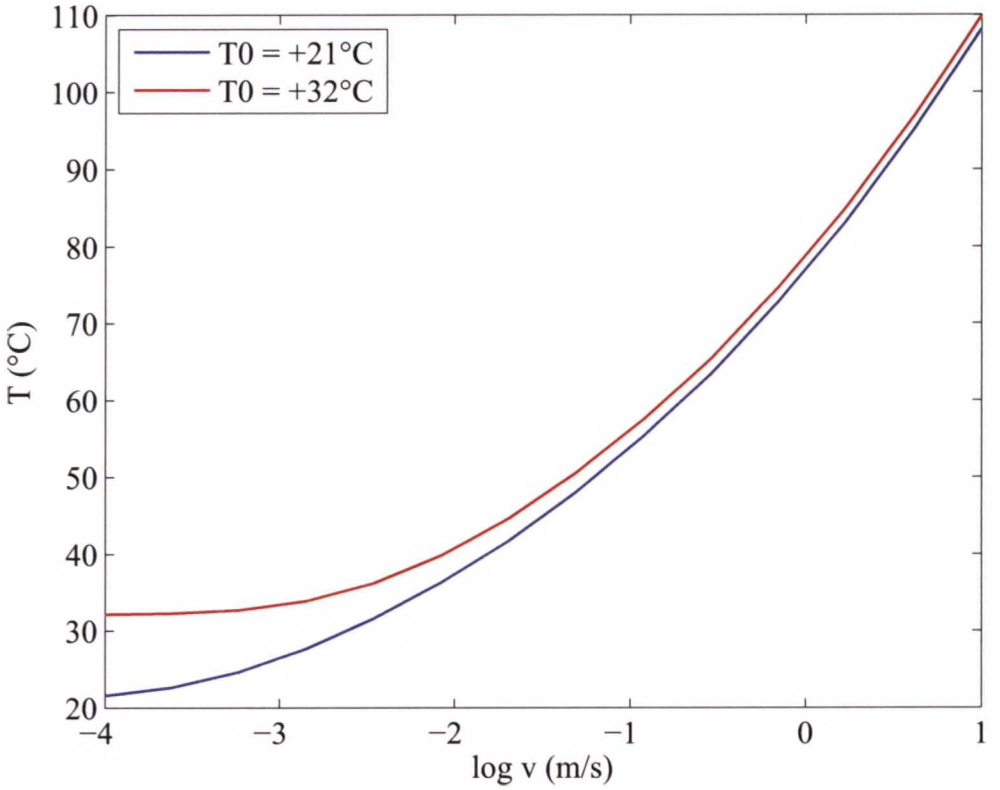

Figure 5.8: The flash temperature for ambient temperatures +21°C and +32°C predicted by the Persson hot friction theory.

When comparing the hot friction model predictions computed using the DMA data to those computed using the SLS model for the viscoelastic modulus, presented in Appendix C, one notes that in the predictions with the SLS model the maximum friction level matches that of the experiments well, being on the order of one, whereas this is not the case with the DMA data, as was noted above. However, recalling that the SLS model is a poor description of real rubber (see Section 2.2.5), the hot friction model with the SLS model should be unreliable. The functional behaviour seems similar for the predictions with DMA data and SLS model. Similar to the predictions using DMA data, also with SLS model, the friction level predicted by the friction model for sliding speeds below that for the maximum friction is too low.

6 Conclusion

In this thesis, the sliding friction exhibited by a rubber-asphalt system was investigated. In particular, the sliding speed dependency of sliding friction for the system was analyzed. A repeatable measurement of the sliding friction for a rubber-asphalt system was demonstrated and the sliding friction was measured for a range of ambient temperatures of T_0 = -8°C – +32°C and sliding speeds $v = 10^{-3}$ m/s – 10^{0} m/s.

The rubber friction theory of Persson from 2006 [5] was implemented in this work and experimental parameters for the surface roughness of the asphalt were measured with optical profilometry and incorporated in the model. Furthermore, the viscoelastic properties of the rubber material used as the slider were incorporated in the theoretical model using DMA data from the manufacturer and interpolating between the measurement points for a continuous spectrum. Additionally, the model was implemented using the Standard Linear Solid (SLS) model for the viscoelastic properties.

It was demonstrated in this work, that unlike older theories such as that from Heinrich and Klüppel in 2000 [7] or Persson's earlier theory from 2001 [8], which do not take into account the build-up of temperature in the rubber during sliding due to frictional heating, known as the *flash temperature effect*, the Persson 2006 theory predicts a qualitatively correct trend for the sliding friction also for sliding speeds on the order of 10^{0} m/s. The flash temperature effect becomes increasingly important at higher sliding speeds, the threshold being the order of 10^{-2} m/s.

For such a low sliding speed also the older theories were applicable, but for applications with high sliding speeds, the new theory from Persson incorporating the *flash temperature effect* can now be used to predict the trend in the sliding friction coefficient. It was noted that the friction level was exaggerated by the model when using DMA data for the viscoelastic properties, but this problem was corrected by fitting a free parameter, to match the maximum friction predicted by the model to that measured in the experiments. This free parameter may account for differences in experimental conditions, such as the humidity, which was not measured. The humidity will affect the water-layer on the surfaces in the climate chamber and hence the adhesion and possible related friction mechanisms.

The friction level was not exaggerated by the friction model when using the SLS model for the viscoelastic properties but as the SLS is a poor description of real rubber, it was not further considered in this work. In a further study, the effect of the viscoelastic properties on the model predictions could be investigated by using rubber samples with different viscoelastic moduli and incorporating their DMA data in the model.

The predictability of the sliding speed dependency of sliding friction using the loss tangent was assessed, and it was noted that, taking into account the flash temperature effect, the loss tangent qualitatively predicts the sliding friction at least up to speeds on the order of 10^{0} m/s. The inability of the Persson model to predict the sliding friction for low sliding speeds below 10^{-2} m/s that was observed for the ambient temperature of +32°C, can be attributed to other energy dissipation mechanisms than the asperity-induced viscoelastic energy dissipation in the bulk, which

are excluded from the model. Such energy dissipation mechanisms include energy dissipation by shearing a thin, confined contamination film and energy dissipation by crack opening at the interface [13].

Indeed, it has been shown recently that a combination of the contribution from the viscoelastic deformations and other energy dissipation mechanisms at the contact area based on shearing explain sliding friction of rubber on asphalt well for a wide sliding velocity range of v = 10^{-7} m/s – 10^{0} m/s [43]. For low sliding speeds below v = 10^{-2} m/s, the contribution to the friction from the area of contact was found to dominate the sliding friction, whereas for speeds higher than v = 10^{-1} m/s, the effect of the viscoelastic deformations dominates.

Thus the conclusion is drawn that the sliding speed dependency of rubber sliding friction can be mostly attributed to the frequency and temperature dependency of the loss tangent for sliding speeds which are higher than the order of 1 cm/s, but the temperature dependency of sliding friction is also affected by other factors, such as shearing at the interface. Hence, to improve the prediction of the overall friction level and sliding speed dependency of sliding friction at low speeds, interface properties such as adhesion should be incorporated in the model.

Furthermore, the average size of the macro-asperities on the surface and the corresponding zooming factor ξ_m, estimated in Appendix A of [5], should be determined experimentally for the asphalt substrate used in the experiments. Also, the values for mass density ρ and heat capacity C_V of rubber were not linked to the samples used in the experiments, but were empirical values for rubber in general from [5]. These factors affect the heat diffusivity in the rubber and thus the local temperatures and the loss tangent and friction.

Also the limits of the self-affinity for the asphalt substrate, especially the short distance cut-off could be studied in more detail and determined experimentally using the AFM, for instance. However, the multiscale approach proved very applicable as it accounts for the many different frequencies, corresponding temperatures in the rubber and the effect on viscoelastic energy dissipation. Finally, in a further study, the effect of humidity and adhesion on sliding friction could be assessed in more detail.

References

[1] V. L. Popov, *Contact mechanics and friction: physical principles and applications* (Springer, 2010).

[2] Y.-z. Hu, T.-b. Ma, and H. Wang, Friction **1**, 24 (2013).

[3] P. Spijker, G. Anciaux, and J.-F. Molinari, Tribology International(2012).

[4] Y. Mo, K. Turner, and I. Szlufarska, Nature **457**, 1116 (2009).

[5] B. Persson, Journal of Physics: Condensed Matter **18**, 7789 (2006).

[6] K. Grosch, Proceedings of the Royal Society of London. Series A. Mathematical and Physical Sciences **274**, 21 (1963).

[7] M. Klüppel and G. Heinrich, Rubber chemistry and technology **73**, 578 (2000).

[8] B. N. Persson, The Journal of Chemical Physics **115**, 3840 (2001).

[9] "Transport: Nanotechnology in automotive tyres," (2011), `http://www.nanopinion.eu/sites/default/files/briefing_no.23_nanotechnology_in_automotive_tyres.pdf`.

[10] I. Lopez, in *Proceedings of the International Conference on Noise and Vibration Engineering ISMA* (2010) pp. 4039–4052.

[11] H. Hertz, Journal für die reine und angewandte Mathematik **92**, 156 (1882).

[12] B. Persson, Surface Science Reports **61**, 201 (2006).

[13] B. Lorenz, *Contact mechanics and friction of elastic solids on hard and rough substrates*, Vol. 37 (Forschungszentrum Jülich, 2012).

[14] J. Greenwood and J. Williamson, Proceedings of the Royal Society of London. Series A. Mathematical and Physical Sciences **295**, 300 (1966).

[15] K. L. Johnson, *Contact mechanics* (Cambridge University Press, 1987).

[16] K. Fuller and D. Tabor, Proceedings of the Royal Society of London. A. Mathematical and Physical Sciences **345**, 327 (1975).

[17] J. Archard, Proceedings of the Royal Society of London. Series A, Mathematical and Physical Sciences **243**, 190 (1957).

[18] K. Johnson, K. Kendall, and A. Roberts, Proceedings of the Royal Society of London. A. Mathematical and Physical Sciences **324**, 301 (1971).

[19] A. Schallamach, Wear **17**, 301 (1971).

[20] J. Israelachvili, *Intermolecular and Surface Forces*, 2nd ed. (Academic Press London, 1992).

[21] J. Katainen, *Surface bonding: From molecules to microparticles*, Ph.D. thesis, Helsinki University of Technology (2007).

[22] B. B. Mandelbrot, "The fractal geometry of nature," (1982).

[23] B. Persson, The Journal of Chemical Physics **115**, 3840 (2001).

[24] B. Persson, O. Albohr, U. Tartaglino, A. Volokitin, and E. Tosatti, Journal of Physics: Condensed Matter **17**, R1 (2005).

[25] D. Roylance, Department of Materials Science and Engineering–Massachusetts Institute of Technology, Cambridge MA **2139**, 1 (2001).

[26] W. N. Findley, J. S. Lai, and K. Onaran, *Creep and relaxation of nonlinear viscoelastic materials: with an introduction to linear viscoelasticity* (Courier Dover Publications, 1976).

[27] "Linear viscoelasticity," `http://academic.csuohio.edu/duffy_s/Linear_Visco.pdf`.

[28] M. L. Williams, R. F. Landel, and J. D. Ferry, Journal of the American Chemical Society **77**, 3701 (1955).

[29] L. Mullins, Rubber Chemistry and Technology **42**, 339 (1969).

[30] J. Diani, B. Fayolle, and P. Gilormini, European Polymer Journal **45**, 601 (2009).

[31] A. Schallamach, Wear **6**, 375 (1963).

[32] Z. Radó, *A Study of Road Surface Texture and its Relationship to Friction*, Ph.D. thesis, The Pennsylvania State University (1994).

[33] S. Westermann, F. Petry, R. HOES, and G. Thielen, KGK. Kautschuk, Gummi, Kunststoffe **57**, 645 (2004).

[34] C. Yang, U. Tartaglino, and B. Persson, The European Physical Journal E **19**, 47 (2006).

[35] B. N. Persson, Surface science **401**, 445 (1998).

[36] B. Hunnekens, "Tire road frictional interaction. Bachelor's thesis, Department of Mechanical Engineering, Dynamics and Control Group, Eindhoven University of Technology," (2008).

[37] GFM, "Portable Street Measuring Systems.." (2013), `http://www.gfm3d.com/index.php?option=com_content&view=article&id=111%3Astrassenmessung&catid=42&Itemid=56&lang=en`.

[38] PerkinElmer, "Introduction to dynamic mechanical analysis (dma)," (2008), http://www.metrotec.es/metrotec/WWW_DOC/GDE_IntroductionToDMA-1-CAT-E-R1.pdf.

[39] PerkinElmer, "Dynamic mechanical analysis basics," (2007), http://www.perkinelmer.com/CMSResources/Images/44-74304app_thermaldynmechanalybasicspart1.pdf.

[40] A. W. Mix and A. J. Giacomin, Polymer-Plastics Technology and Engineering **50**, 288 (2011).

[41] Y. Fukahori, P. Gabriel, and J. Busfield, Wear **269**, 854 (2010).

[42] C. H. Reinsch, Numerische mathematik **10**, 177 (1967).

[43] B. Lorenz, B. Persson, G. Fortunato, M. Giustiniano, and F. Baldoni, Journal of Physics: Condensed Matter **25**, 095007 (2013).

[44] A. J. Tuononen, Tribology International(2013).

Appendices

A MATLAB routines for Persson friction model

This implementation requires MATLAB R2012b and tabulated data for the viscoelastic modulus as a function of frequency.

A.1 run_model.m

```
%% Set model constants
rubber = struct;
rubber.nu = 0.5; % Poisson ratio
rubber.rho = 1000; % Mass density
rubber.C_V = 1000; % Heat capacity
rubber.D = 1e-7; % Heat diffusivity
rubber.E1 = 1e9; % Real modulus
rubber.Tg = -16; % Glass transition temp (Celsius)
% DMA data
load('DMA.mat');
rubber.DMA_omega = DMA_omega_using_WLF;
rubber.DMA_E = DMA_E;

substrate = struct;
substrate.H = 0.84; % Hurst exponent
substrate.q_0 = 800; % Roll-off wavevector
substrate.h_0 = 1/substrate.q_0; % % Rms roughness amplitude
substrate.k = (substrate.h_0/substrate.q_0)^2*substrate.H/(2*pi);
substrate.ksii_m = 3.5; % Macro-asperity zooming factor

contact = struct;
contact.sigma_0 = 0.14e6; % Contact pressure
contact.T0 = 32; % Ambient temperature (Celsius)

%% Compute the flash temperatures Tq for all q and v
number_of_v = 15;
v_vector=logspace(-4,1,number_of_v);
q = logspace(log10(substrate.q_0), log10(400*substrate.q_0), 100);
Tq = zeros(length(v_vector),length(q));
aT = zeros(length(v_vector),length(q));

if (matlabpool('size') == 0)
    matlabpool open
end
parfor i = 1:number_of_v
    [Tq(i,:), aT(i,:)] = flash_temp(q,v_vector(i), rubber, substrate, contact);
    Tq(i,:)
    disp([num2str(i/number_of_v*100), ...
    ' % done of Tq calc for v (previous v = ', num2str(v_vector(i)), ')'])
end
if (matlabpool('size') ~= 0)
    matlabpool close
end

```

```
%% Compute friction coefficients as a function of v and xi
mu_cold_var_v=zeros(size(v_vector));
mu_hot_var_v=zeros(size(v_vector));
for i = 1:length(v_vector)
        mu_cold_var_v(i) = compute_mu(q,v_vector(i),WLF(contact.T0,rubber),...
            rubber, substrate, contact);
        mu_hot_var_v(i) = compute_mu(q,v_vector(i),aT(i,:),...
            rubber, substrate, contact);
end

mu_cold_var_xi = zeros(size(q));
mu_hot_var_xi = zeros(size(q));
for i = 1:length(q)
    mu_cold_var_xi(i) = compute_mu(q(1:i),1,WLF(contact.T0,rubber),...
            rubber, substrate, contact);
    mu_hot_var_xi(i) = compute_mu(q(1:i),1,aT_v1(1:i),...
            rubber, substrate, contact);
end
```

A.2 flash_temp.m

```
function [ Tq_, aT_ ] = flash_temp( q, v, rubber, substrate, contact )
% Calculate macroasperity radius R_asp
% Set constants a,b,c
a_const = 0.526; b = 3.636; c = 0.729; % [5] Appendix A
a_T0 = WLF(contact.T0, rubber);
Pq_m = P_numerical_mex(substrate.q_0*substrate.ksii_m,v,a_T0,rubber,...
   substrate,contact);
R_asp = (a_const + b * Pq_m^c)/(substrate.ksii_m * substrate.q_0);
% Calculate half-contact time t0
t0 = R_asp / v;

%% Compute matrix g(q,q')
% Denote Persson 2006 q' by q_ in the code
q_ = logspace(log10(substrate.q_0), log10(400*substrate.q_0), 300);
g = zeros(length(q),length(q_));
D = rubber.D;
for i = 1 : length(q)
    Q = q(i);
    for j = 1 : length(q_)
        g(i,j) = 1/pi*quadgk(@(k)1./(D*k.^2).*(1-exp(-D*k.^2*t0))*...
            4.*q_(j)./(k.^2 + 4*q_(j).^2)*4.*Q.^2./...
            (k.^2 + 4*Q.^2),0,Inf);
    end
end

%% Tq loop
Tq_ = zeros(size(q));
aT_ = zeros(size(q));
% Use contact.T0 as the starting temperature for q(1)
[Tq_(1), aT_(1)] = compute_Tq(1,contact.T0, v, g, q_, Pq_m,rubber,...
    substrate,contact);
for i = 2:length(q)
```

```
33      [Tq_(i), aT_(i)] = compute_Tq(i,Tq_(i-1), v, g, q_, Pq_m,rubber,...
34          substrate,contact);
35  end
36  end
```

A.3 WLF.m

```
1  function [a] = WLF(T, rubber)
2  % WLF uses the Williams-Landel-Ferry equation to approximately describe
3  % the temperature dependence of the viscoelastic modulus
4
5  log10aT = -8.86*(T - rubber.Tg - 50)./(51.5 + T - rubber.Tg);
6  a = 10.^(log10aT);
```

A.4 P_numerical.m

```
1  function P = P_numerical(q, v, aT, rubber, substrate, contact)
2  if (length(q) == 1)
3      q_range = logspace(log10(substrate.q_0), log10(q), 100);
4      G = 1/8*trapz(q_range, G_integrand(q_range,v,aT,rubber,substrate,...
5          contact));
6      P = erf(1/(2*sqrt(G)));
7  else
8      P=zeros(size(q));
9      P(1) = 1;
10     for index=2:length(q)
11         q_range = q(1:index);
12         if (length(aT) == 1)
13             G = 1/8*trapz(q_range, G_integrand(q_range,v,aT,rubber,...
14                 substrate, contact));
15         else
16             G = 1/8*trapz(q_range, G_integrand(q_range,v,aT(1:index),...
17                 rubber, substrate, contact));
18         end
19
20         P(index) = erf(1/(2*sqrt(G)));
21
22     end
23 end
24 end
```

A.5 G_integrand.m

```
1  function G_int = G_integrand(q, v, aT, rubber, substrate, contact)
2  % G_integrand is the integrand in the equation for G(q)
3
4  C_q=C(q, substrate);
5  G_int=q.^3.*C_q.*E_integral(q,v,aT,rubber, contact);
6  end
```

A.6 E_integral.m

```
function E_int = E_integral(q, v, aT, rubber, contact)
nu = rubber.nu;
sigma_0 = contact.sigma_0;

phi=0:2*pi/100:2*pi;
q=q.*aT;
omega=q'*v*cos(phi);

E = zeros(size(omega));
E = complex(E,0);
size_E = size(E);
for i = 1:size_E(1)
    E(i,:) = E_DMA(omega(i,:), rubber);
end

E_int = trapz(phi,abs(E)/((1-nu^2)*sigma_0).^2,2)';
end
```

A.7 E_DMA.m

```
function [ E ] = E_DMA( omega, rubber )
%E_DMA Interpolates linearly between DMA measurement points
    % If omega is outside the measurement range, Standard Linear Solid
    % model is used to approximate the value of E

ReE = interp1(rubber.DMA_omega,rubber.DMA_E(:,1), omega);
ImE = interp1(rubber.DMA_omega,rubber.DMA_E(:,2), omega);

Re = zeros(size(omega));
E = complex(Re,0);
for i = 1:length(omega)
    if (¬isnan(ReE(i)))
        E(i) = complex(ReE(i), ImE(i));
    else
        E(i) = rubber.E1*(1-1i*omega(i).*rubber.tau)./...
            (1+rubber.a-1i*omega(i)*rubber.tau);
    end
end
end
```

A.8 compute_Tq.m

```
function [ Tq, aT ] = compute_Tq( q_index, Tq_prev, v, g, q_, Pq_m, ...
    rubber, substrate, contact)
% Returns the temperature Tq and corresponding shift factor aT for
% wavenumber corresponding to q_index

Tq_low = Tq_prev - 1;   % The temperature can only increase, not decrease,
```

```
7                           % as a result of friction, however due to the
8                           % numerics, Tq_low has to be small enough
9  Tq_high = Tq_prev + 100; % Must be high enough
10
11 % Define a tolerance for the iteration
12 TOL = 10^-3;
13
14 aT = WLF(Tq_low,rubber);
15 P = P_numerical_mex(q_, v, aT, rubber, substrate, contact);
16 f = v*q_.^4./(rubber.rho*rubber.C_V).*C(q_, substrate).*...
17             P./Pq_m .* f_integral( q_, v, aT, rubber );
18 RHS = contact.T0 + trapz(q_,g(q_index,:).*f*(-1),2);
19 difference_Tq_low = RHS - Tq_low;
20
21 aT = WLF(Tq_high,rubber);
22 P = P_numerical_mex(q_, v, aT, rubber, substrate, contact);
23 f = v*q_.^4./(rubber.rho*rubber.C_V).*C(q_, substrate).*...
24             P./Pq_m .* f_integral( q_, v, aT, rubber );
25 RHS = contact.T0 + trapz(q_,g(q_index,:).*f*(-1),2);
26 difference_Tq_high = RHS - Tq_high;
27
28 % MAKE SURE THAT sign(difference_Tq_low) != sign(difference_Tq_high)
29 if sign(difference_Tq_low) == sign(difference_Tq_high)
30     disp('ERROR: sign(difference_Tq_low) == sign(difference_Tq_high)')
31     sign(difference_Tq_low)
32     sign(difference_Tq_high)
33 end
34 number_of_iterations = 0;
35 while 1
36     number_of_iterations = number_of_iterations + 1;
37     if (number_of_iterations > 100)
38         disp('ERROR: No convergence')
39         break;
40     end
41     % Calculate a new midpoint
42     Tq = (Tq_low + Tq_high) / 2;
43
44     % Calculate the shift factor aT for the last temperature using WLF
45     aT = WLF(Tq,rubber);
46     P = P_numerical_mex(q_, v, aT, rubber, substrate, contact);
47     f = v*q_.^4./(rubber.rho*rubber.C_V).*C(q_, substrate).*...
48             P./Pq_m .* f_integral( q_, v, aT, rubber );
49
50     % Calculate the new temperature Tq
51     RHS = contact.T0 + trapz(q_,g(q_index,:).*f*(-1),2);
52     difference = RHS - Tq;
53
54     % Apply the bisection method
55
56     % Check if difference has the same or opposite sign for Tq_low and
57     % Tq_value
58     if sign(difference_Tq_low) == sign(difference)
59         Tq_low = Tq;
60         difference_Tq_low = difference;
```

```
61      else
62          Tq_high = Tq;
63      end
64      % Check if solution found
65      if (Tq_high - Tq_low) / 2 < TOL
66          Tq = (Tq_low + Tq_high) / 2;
67          aT = WLF(Tq,rubber);
68          break
69      end
70  end
```

A.9 C.m

```
1  function C_value = C(q, substrate)
2  % Calculates C(q) according to the power law for self-affine surfaces
3
4  C_value=substrate.k*(q./substrate.q_0).^(-2*(substrate.H+1));
5  end
```

A.10 f_integral.m

```
1  function [ f_integral ] = f_integral( q, v, aT, rubber )
2  nu = rubber.nu;
3
4  phi=0:2*pi/100:2*pi;
5  q=q.*aT;
6  omega=q'*v*cos(phi);
7
8  E = zeros(size(omega));
9  size_E = size(E);
10 for i = 1:size_E(1)
11     E(i,:) = E_DMA(omega(i,:), rubber);
12 end
13
14 E_imag = imag(E);
15 integrand = zeros(size(E_imag));
16 cos_phi = cos(phi);
17 for i = 1:size_E(1)
18     integrand(i,:) = cos_phi.*E_imag(i,:)/(1-nu^2);
19 end
20
21 f_integral = trapz(phi,integrand,2)';
22 end
```

A.11 compute_mu.m

```
1  function mu = compute_mu(q,v,aT, rubber, substrate, contact)
2  mu = 1/2*trapz(q, q.^3.*C(q,substrate).*P_numerical(q,v,aT,rubber,...
3      substrate,contact).*f_integral(q,v,aT,rubber)*(-1)/contact.sigma_0,2);
4  end
```

B Pseudocode of solving for the flash temperature

To solve for the flash temperature T_q for each roughness wavenumber q in equations (54) – (56), the bisection method is used. Pseudocode for the solution is presented in Algorithm 1.

Algorithm 1 Numerically solving for $T_q(q, v)$

$q_{array} \leftarrow \{q_0 : \xi_{max} * q_0\}$; ▷ run_model.m A.1
for all v **do**
  set ξ_m, R_{asp}; ▷ flash_temp.m A.2
  $t_0 \leftarrow R_{asp} \,/\, v$;
  $q'_{array} \leftarrow \{q_0 : \xi_{max} * q_0\}$;
  for all q in q_{array} **do**
    for all q' in q'_{array} **do**
      compute $g(q, q')$; ▷ Eq. (55)
    end for
  end for
  initialize T_{q_array} and aT_{array} to length(q);
  compute $T_{q\_array}(1)$ and $aT_{array}(1)$ as below, but using T_0 as the initial guess
  for $i = 2 \rightarrow$ length(q) **do**
    $T_{q\_low} \leftarrow T_{q\_array}(i-1) - 1$; ▷ compute_Tq.m A.8
    $T_{q\_high} \leftarrow T_{q\_array}(i-1) + 100$;
    $diff\_T_{q\_low} = T_q(T_{q\_low}) - T_{q\_low}$; ▷ $T_q()$ in Eq. (56)
    $diff\_T_{q\_high} = T_q(T_{q\_high}) - T_{q\_high}$;
Require: sign($diff\_T_{q\_low}$) $\neq$ sign($diff\_T_{q\_high}$)
    $TOL \leftarrow 10^{-3}$; ▷ Set a tolerance
    while $(T_{q\_high} - T_{q\_low}) \,/\, 2 > TOL$ **do**
      $T_{q\_current} \leftarrow (T_{q\_low} + T_{q\_high}) \,/\, 2$;
      $aT_{array}(i) =$ WLF($T_{q\_current}$); ▷ WLF.m A.3
      compute $P(q)$; ▷ P_numerical.m A.4
      compute $f(q)$; ▷ Eq. (54), f_integral.m A.10
      $diff\_T_q \leftarrow T_q(T_{q\_current}) - T_{q\_current}$; ▷ $T_q()$ in Eq. (56)
      if sign($diff\_T_{q\_low}$) == sign($diff\_T_q$) **then**
        $T_{q\_low} \leftarrow T_{q\_current}$; ▷ Solution in upper half of T_q range
        $diff\_T_{q\_low} \leftarrow diff\_T_q$;
      else
        $T_{q\_high} \leftarrow T_{q\_current}$; ▷ Solution in lower half of T_q range
      end if
    end while
    $T_{q\_array}(i) \leftarrow (T_{q\_low} + T_{q\_high}) \,/\, 2$; ▷ Solution found
    $aT_{array}(i) \leftarrow$ WLF($T_{q\_array}(i)$);
  end for
  save T_{q_array} and aT_array for current v;
end for

C Results from Persson model with SLS

A comparison between measurement results and the Persson cold friction and hot friction models are presented in figures C1 and C2 at ambient temperatures of +21°C and +32°C, respectively. The SLS model is used for the viscoelastic modulus, whereas other parameters are the same as in Table 5.6. One notes that the Persson hot friction model predicts the sliding friction coefficient qualitatively correctly and the level of maximum friction is also on the same order of magnitude as for the experiments.

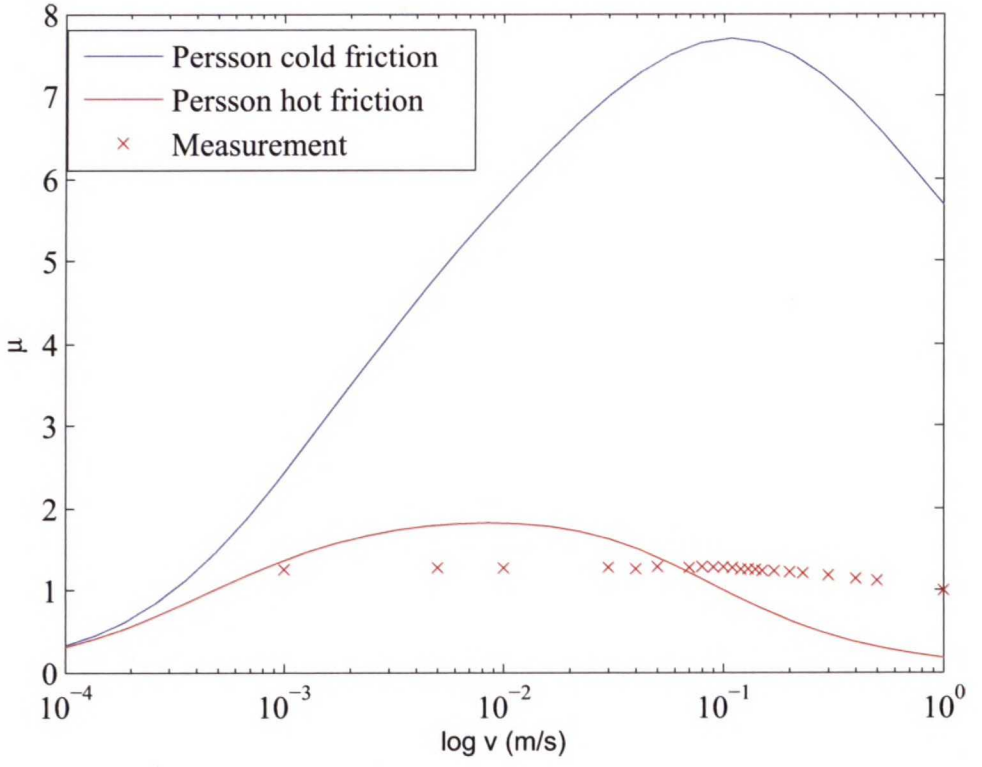

Figure C1: Comparison of Persson rubber friction models with experiment at +21°C using the SLS model for the viscoelastic modulus.

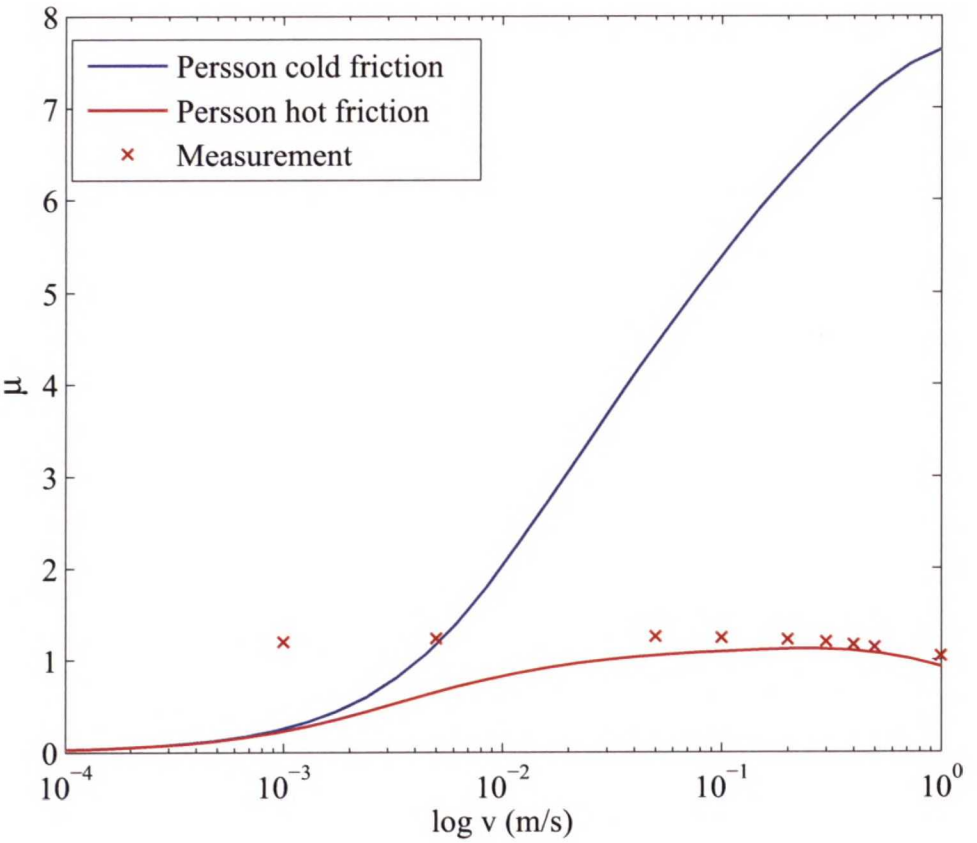

Figure C2: Comparison of Persson rubber friction models with experiment at +32°C using the SLS model for the viscoelastic modulus.

D Analysis of vibrations in the linear friction tests

The resonant vibration is only observed for combinations of temperatures, which are higher than -8°C, and sliding speeds, which are higher than 200 mm/s. Such resonance can be observed, for instance, at +21°C for a sliding speed of 400 mm/s but not so clearly at 300 mm/s, as shown in Fig. D1a, and even less so below 300 mm/s. Resonant vibration is also clearly observable for sliding speeds of 500 mm/s and 1000 mm/s, as seen in Fig. D1b, and the vibration is greater in amplitude for the higher speeds. Overall, the higher the temperature and the sliding speed, the greater the amplitude of the resonant vibration.

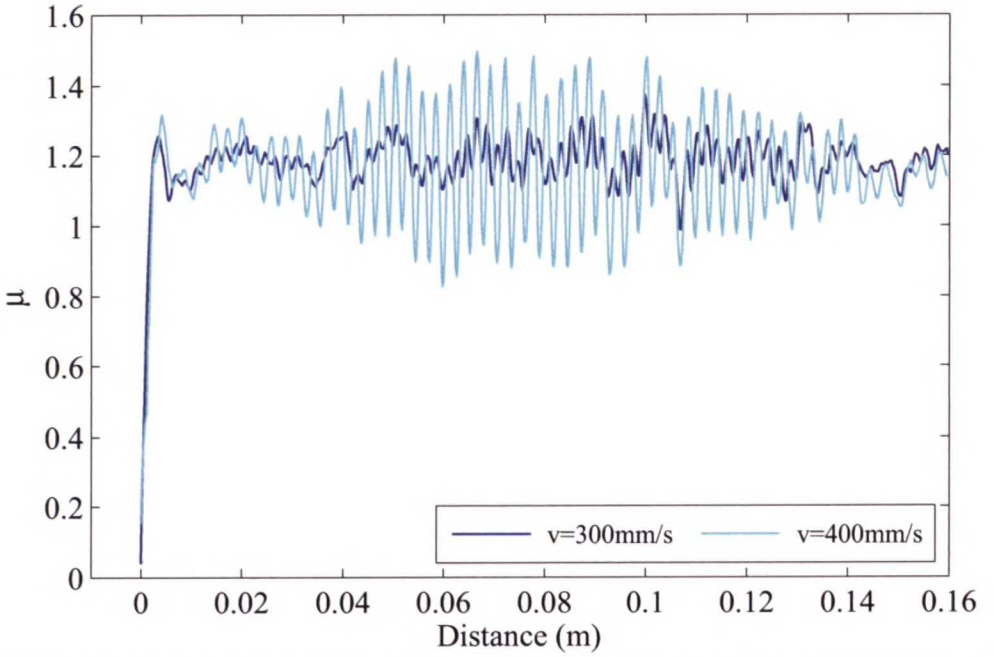

(a) Sliding speeds 300 mm/s and 400 mm/s. Resonant vibration with an enhanced amplitude starts at v = 400 mm/s.

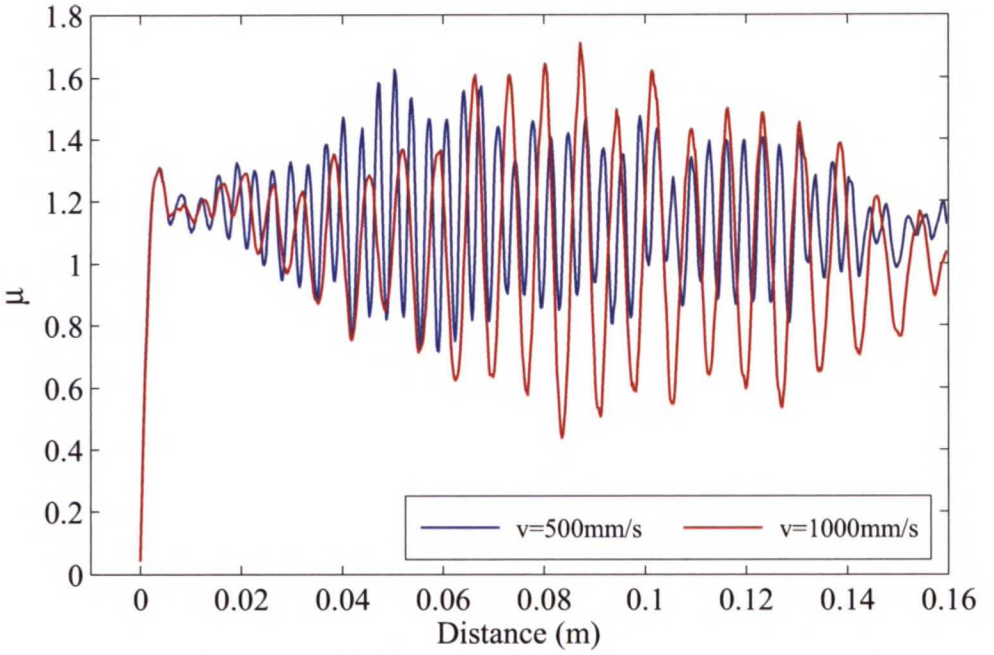

(b) Sliding speeds 500 mm/s and 1000 mm/s. Both speeds show resonance similar to that of v = 400 mm/s in (a) with an enhanced amplitude.

Figure D1: Friction coefficient versus sliding distance at +21°C during the first temperature cycle. Resonant vibration is observable for sliding speeds 400 mm/s, 500 mm/s and 1000 mm/s.

To explore the frequencies of vibration in the above measurements, we carried out spectral analysis for the distance-domain signals by calculating the power spectral density (PSD) using the Welch method. Figure D2 shows the PSD of the friction test with v = 1000 mm/s at +21°C with sample S1. As can be seen in the figure, the PSD curve reveals two major components, one at approximately 135 Hz and the other at approximately 320 Hz. The 135 Hz frequency is clearly the most abundant, with a difference of more than two orders of magnitude in the PSD to the 320 Hz frequency.

These two major components are present in the PSD of the friction tests for all sliding speeds featured in Fig. D1, with the peak frequencies within ±10 Hz from the values stated for v = 1000 mm/s above. The most abundant frequency of 135 Hz has also been observed when measuring rubber friction on glass in another study using the same apparatus [44]. Thus, we conclude that this frequency arises in the whole apparatus as a complete vibrating system including the table, which the linear friction tester is mounted on, rather than in the rubber material of the samples as a result of the rough asphalt substrate only.

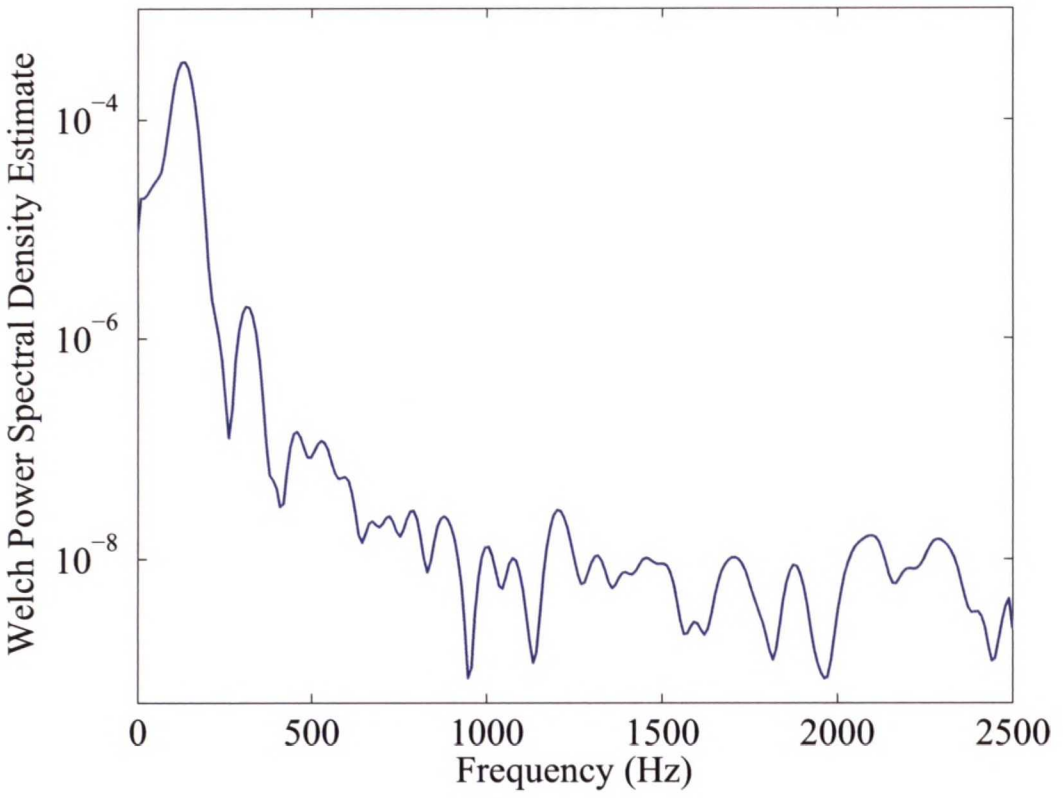

Figure D2: PSD computed using the Welch method for the μ vs. distance curve of Fig. D1b with v = 1000 mm/s at +21°C .

E Wear of rubber samples in the measurements

Photographs of samples S4 and S5 after the measurements are presented in Fig. E1. S4 was used in Lines in the sliding direction caused by wear can be clearly seen on the rubber surface for both samples. The sliding direction is indicated by the black arrow on the aluminum sample holder. We also note that the leading edge, which is the right edge in the figure, is clearly worn out in sample S4 (see the leading edge of S4 in Fig. E1a and the leading edge of S4 from a different angle in Fig. E1b on the left side of S5), whereas this is not the case for sample S5, as seen in Fig. E1b. The wear is similar for samples S1–S3 as for S4, although S4 was used at two temperatures, whereas S1–S3 at only one temperature, so S4 was slid two times as much.

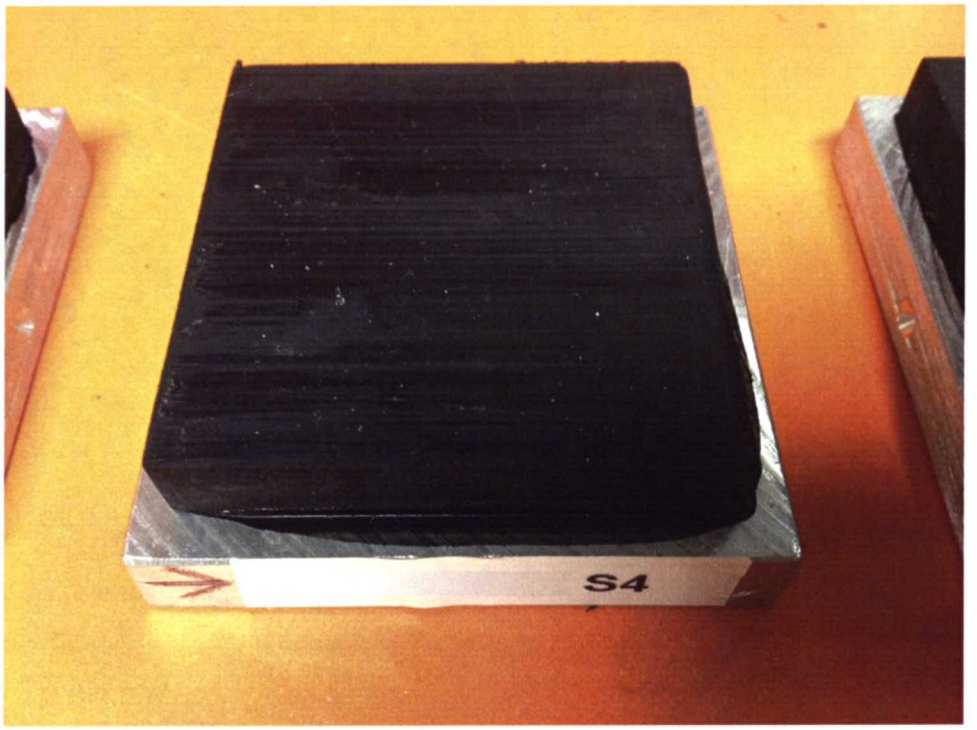

(a) Sample S4 after all measurements. Lines in the sliding direction (indicated by the black arrow at the bottom left corner of the image, on the aluminum sample holder) caused by wear can be seen on the rubber surface.

(b) Sample S5 after run-in. S5 is used as the reference and no further measurements were carried out using this sample after the run-in.

Figure E1: Photographs of samples S4 and S5.

F Asphalt roughness profile

The power spectrum averaged over 10 measurements, each taken from a different spot on the asphalt with the GFM, is shown in Fig. F1. The spectrum exhibits self-affinity as expected. By fitting lines to the measured spectrum, we obtained values of $H = 0.84$ and $q_0 = 800$ for the Hurst exponent and roll-off wavevector, respectively.

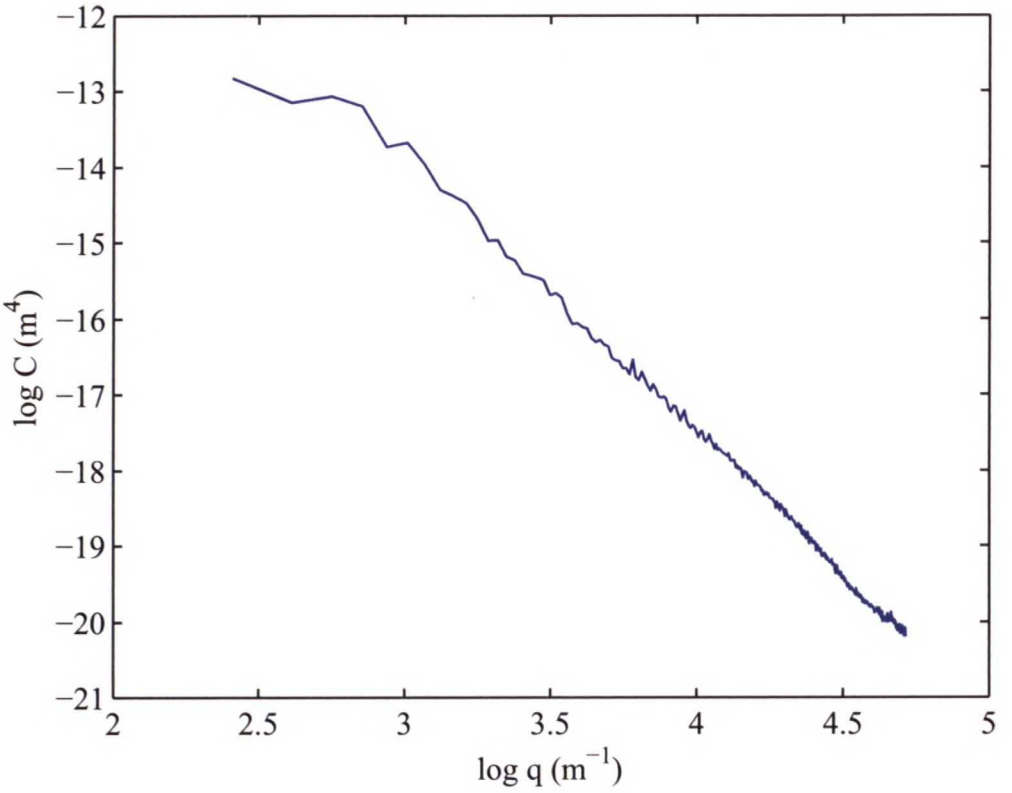

Figure F1: Power spectrum of the asphalt surface used in the linear friction tests with $H = 0.84$ and $q_0 = 800$.